

Liquid flow-focused by a gas: jetting, dripping and recirculation

Miguel A. Herrada, Alfonso M. Gañán-Calvo, Antonio
Ojeda-Monge, Benjamin Bluth, Pascual Riesco-Chueca

E.S.I, Universidad de Sevilla.

Camino de los Descubrimientos s/n 41092 Spain.

(Dated: May 24, 2022)

Abstract

Flow-focused liquid jetting by gas is explored by (a) experiment and (b) direct axisymmetric VOF numerical simulation. The cone-jet flow pattern is seen to evolve as we modify the liquid flow-rate around the jetting-dripping transition. As observed in other focused flows like electrospraying cones upon steady thread emission, the flow displays a strong recirculating pattern within the conical meniscus; it is shown to play a role on the stability of the system, being a precursor to incipient dripping. Close to the minimum liquid flow rate for steady jetting, the recirculation cell penetrates into the feed tube. Both the jet diameter and the size of the cell are accurately estimated by a simple theoretical model. In addition, the transition from jetting to dripping is numerically analyzed in detail in some illustrative cases, showing remarkable agreement with experiments.

I. INTRODUCTION

The controllable production of small flowing geometries is a crucial challenge for chemical engineering [1] and bio-industry. Drops, bubbles, jets and recirculation cells in the micro-scale provide a useful platform for diverse technical applications. Here we concentrate on cone-jet flow patterns, looking at the streamline geometry in the jetting to dripping transition. An elusive phenomenon, recirculating flow, is shown to take place just before the transition. The conditions for such occurrence are extremely interesting, both as an indicator phenomenon associated to the jetting-dripping threshold, and as an attractive technological feature.

Small droplet generation by means of co-flowing immiscible fluid streams has become widespread. The intrinsic smallness of the output droplets generally leads to small Reynolds number flows. Thus, a number of classic studies back to Taylor [2] including the recently blooming field of co-flowing microfluidics take the low Reynolds number assumption for granted. For example, a beautifully simple scheme (a straight tube surrounds a coaxial, more slender tube, two immiscible fluids being fed through each tube) has been thoroughly explored by Suryo and Basaran [3] using a computer simulation: they show that a locally extensional flow spontaneously develops at the tip of the elongated drop drawn by the co-flowing liquid, causing the seemingly continuous ejection of extremely small droplets by tip streaming under certain parametrical combinations. This is obtained without the burden of complex geometry. It is hoped, therefore, that low Reynolds co-flowing small-droplet generation may become a hydrodynamic standard in a near future. Different setups have been proposed where the flow is driven by an external straining flow. Among them, the elegant analytical solution by Zhang [4], points to parametrical combinations where extremely thin fluid jets, even down to the molecular scale, could be continuously reached. Those jets, if confirmed, would yield unimaginably small droplets upon breakup.

In spite of their generality and tractability, low Reynolds number flows are constrained by the requirement that the overall flow velocity does not grow above a certain threshold to ensure that inertial forces remain negligible. This constraint limits the overall productivity of low-Re systems. Co-flowing with inertia was successfully explored, aiming at a reduction of the issued bubble diameter, by Oguz and Prosperetti[5]. Subsequently, new perspectives were open by the emergence of moderate-high Reynolds flow-focusing [6] as

a high-productivity alternative to low Reynolds co-flowing systems. Compared to other co-flowing techniques, flow focusing (FF) stands today as a mature microfluidic standard yielding steady capillary jets or droplets whose size is well below the scale of the flow boundaries. As originally conceived, FF aimed at the generation [6] of continuous steady micro-jets upon focusing by a co-flowing gas stream at moderate-high Reynolds number. Furthermore, FF was shown [7] to produce perfectly monodisperse microbubble streams when the co-flowing current is a liquid. A slight variation of the concept was subsequently introduced by Takeuchi et al. [8] to produce microbubbles. When the axisymmetric geometry originally proposed was reduced to a planar topology [9], particularly suitable for microfluidics, the scientific literature production on flow focusing underwent a enormous boost[10, 11, 12]. In addition, axisymmetric multiple-phase FF leading to compound co-axial microjets (Ganan-Calvo 1998[6], page 288) has been developed by other authors to produce microcapsules in a microfluidic setup at relatively low [13] and moderate Reynolds numbers[14].

The technological applications of FF in industry were evident from its very inception. A crucial advance resulted from the combination of massive production (high production rates of microscopic fluidic entities) and accurate tailoring. Indeed, depending on the fluid combination topology (a decision determining which interfaces are to be created), the nature of the fluids involved, gas or liquid, and the system geometry, an output including nearly monodisperse micro-droplets, bubbles or complex capsules can be obtained at an unprecedentedly controllable rate. Surface tension becomes a paramount ally in the ultimate conformation of discrete (generally spherical) fluidic units. Capillary jets have long ago been observed to give rise to continuous drop streams at fast emission rate upon Rayleigh axisymmetric breakup. Here, although surface tension is negligible compared to other driving forces in the global scale, it becomes the main driving agent for jet instability and breakup. Obtaining a jet is therefore the precondition for the creation of a new fluidic scenery with higher velocities and smaller dimensions at no cost in terms of control; and surface tension is free to perform its conformation task in this new scale. Thus, as first proposed in FF, the steady capillary thin jet conformed by pressure forcing by an immiscible co-flowing fluid provides favorable local conditions, a *floating lab* for the generation of bubbles, capsules or droplets.

A FF capillary jet is driven by three main forces: fluid inertia, viscosity and surface tension. Owing to the simplicity of the slender jet geometry, which asymptotically renders all forces strictly additive in one dimension, FF can be scaled with the help of two

dimensionless parameters: (i) the inertia to surface tension forces ratio (Weber number) and (ii) the viscous to surface tension ratio (Capillary number). Other classic numbers such as Reynolds are combinations of the former. Nevertheless, as early noticed [6], an intrinsic feature of FF, namely the presence of a focusing fluid, gives rise to supplementary influences issuing from the correlation between the properties of the focusing and focused fluids. In particular, when the focusing and focused fluids are a gas and a liquid, respectively, the gas sheath flows much faster than the liquid jet at the exit orifice (Fig. 1). Thus, in addition to the extensional viscous forces at the highly stretching region joining the meniscus and the jet, transversal viscous diffusion of momentum causes a non-trivial axial velocity profile. A number of simplifying assumptions have been adopted, yielding accurate first order solutions [6, 15, 16]. However, they are not applicable to predict critical phenomena like the onset of steady jetting, or the jetting-dripping transition, as a function of the working parameters. These problems have been made analytically tractable at the expense of a drastic geometry simplification, i.e. assuming infinite jet slenderness [17, 18, 19]. Such simplified models are predictive in a variety of situations, but FF systems exhibit an intrinsically three-dimensional meniscus from which the jet or the small droplets issue. Simultaneous modelling of the meniscus and the jet goes beyond the scope of present theoretical frameworks. Thus, numerical simulation or experiment are the only avenue to discern the physics of the fluid emission and its parametric conditions. Some further insight can be gained by general scaling laws. This is the approach chosen for the research presented here.

Many authors have applied numerical simulation [20] to this class of problems, where it has supplied welcome information on the droplet dynamics of complex flows [21]. A significant number of studies have been proposed on microfluidic FF devices; occasional comparison with experimental data is provided to validate the numerical model. A liquid-liquid configuration for the production of microemulsions has been simulated [22] to good agreement with experiments [9]. Other authors have considered the microbubbling setup [12, 23], where good experimental fit is also obtained [10].

In this work, we make use of numerical simulation and experiments to study the generation of a liquid jet focused by gas in an axisymmetric FF device, at moderate-high Reynolds numbers. The jet diameters obtained in the simulation are in good agreement with our experiments and scaling laws [6], a fact that fully validates our hypotheses. Among other findings, we determine the flow rate at the jetting-dripping transition for two combinations

of Reynolds and Weber numbers. We observe that either the jet or the cusp-like meniscus are responsible for the global instability of the system, which drives it into well defined dynamical cycles (global dripping). A detailed description of the flow pattern sheds light on the physics of the jetting-dripping transition.

One of the key findings of the simulation is the occurrence, under favorable driving conditions, of a recirculation cell in the meniscus. This is in perfect analogy to recirculating meridian fluid flows observed inside Taylor cones when electrospraying liquids with sufficiently large values of both the viscosity and the electrical conductivity [24, 25]. Additionally, in experiments aiming at the production of tip streaming patterns in liquid-liquid two-dimensional FF (surfactant treated interface), the streamline image of fluorescent particles seeding the flow of the internal, aqueous liquid during thread formation, was shown to consist of symmetric recirculation vortices [26]. In both types of motion, either driven by the electrical stresses acting at the cone surface or by the external focusing flow, the liquid flows towards the meniscus (cone) tip, along the generatrix, and away from it along the axis. The problem under consideration here is comparable to these other instances of recirculating cell, because the driving role of the gas sheath, giving rise to strong tangential forcing at the interface, plays a similar role to either tangential electric stress[24, 25], surfactant-aided liquid-liquid interaction[26], or purely surfactant-driven tip-streaming.[27, 28] In this work, scaling arguments are developed to describe the size and occurrence of purely FF recirculation cells.

II. MATHEMATICAL FORMULATION

The axisymmetric flow-focusing device and the computational domain used are sketched in Fig. 1. A constant liquid flow rate Q_l , flowing through a capillary tube (outer diameter $D_2 = 2R_2$, inner diameter $D_1 = 2R_1$), is forced through a coaxial round orifice of diameter $D = 2R$ (nozzle) located at a downstream distance H from the tube outlet. The liquid stream is drawn by a constant flow rate Q_g of focusing gas stream discharging through the nozzle into a infinitely large chamber. The gas flow is assumed incompressible, in asymptotic consistency with the low pressure drop at the exit orifice, a condition prevailing when maximum droplet size monodispersity is required. Therefore, the incompressible, axisymmetric and unsteady Navier-Stokes equations in cylindrical (z, r, ϕ) coordinates are

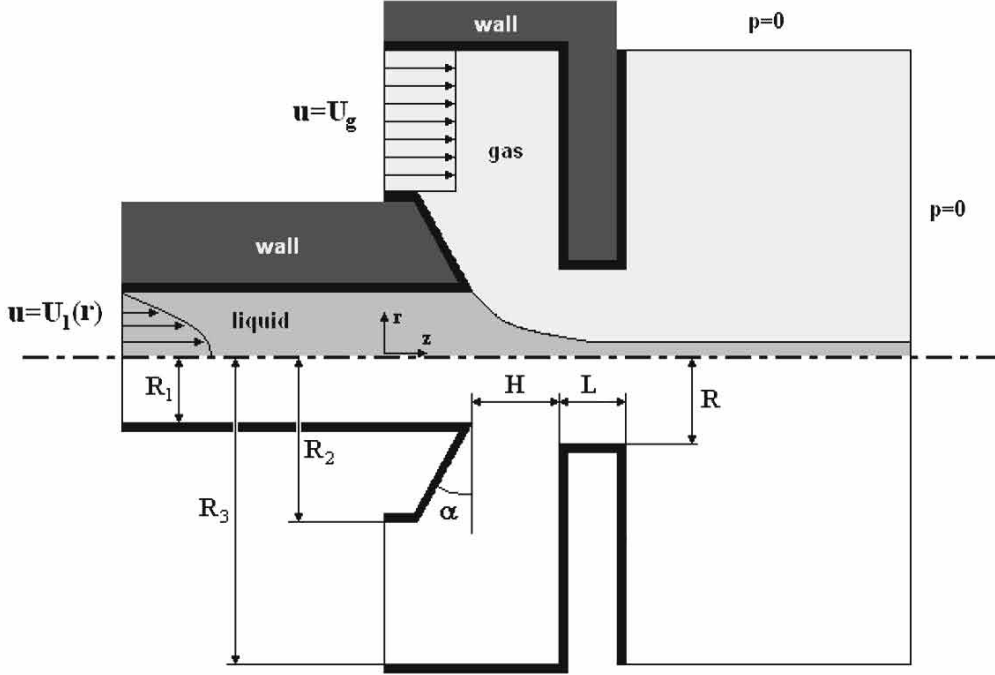


FIG. 1: Simulated boundary geometry and fluid flow domains.

used to describe the time evolution of both fluids.

Fig. 1 also shows the boundary conditions: a) at the liquid inlet, $z = -z_l$, a Hagen-Poiseuille profile, $U_l(r) = V_1[1 - (r/R_1)^2]$, is specified; b) at the gas inlet, $z = 0$, $R_2 < r < R_3$, a uniform axial flow, $U_g(r) = V_2$, is assumed; d) on all solid walls we assume no slip $\mathbf{u} = \mathbf{0}$; e) at the axis $r = 0$ a symmetry condition is applied. The outlet discharge chamber has been modeled as a rectangular box, $z = z_{out}$ and $r = r_{out}$ being two open surfaces where the pressure is set to zero. Note that the corresponding gas and liquid flow rates are related with the imposed inlet velocity field by:

$$Q_l = \int_0^{R_1} 2\pi r U_l(r) dr; \quad Q_g = \int_{R_2}^{R_3} 2\pi r U_g(r) dr. \quad (1)$$

Parametric studies of the dimensionless variables involved are carried out next. The velocity field $\mathbf{u} = (u, v)$ is scaled with the mean gas velocity at the nozzle $V = Q_g/(\pi R^2)$,

while length is scaled with the nozzle radius R , time t with R/V , and pressure p with $\rho_g V^2$, ρ_g being the density of the focusing gas. A single geometrical configuration is considered in this work, characterized by the following aspect ratios: $R_1/R = 0.75$, $R_2/R = 1.75$, $R_3/R = 3.5$, $H/R = 1$ and $L/R = 0.75$. We have chosen a liquid-gas combination where

$$\frac{\rho_l}{\rho_g} = 833.33, \frac{\mu_l}{\mu_g} = 55.55 \quad (2)$$

ρ and μ being the density and viscosity of the liquid (subindex l) and the gas (g). This choice is representative of the experimental jetting of air-focused water. The problem is governed by the following dimensionless parameters: Reynolds and Weber numbers

$$Re = \frac{\rho_g V R}{\mu_g}, \quad (3)$$

$$We = \frac{\rho_g V^2 R}{\sigma}; \quad (4)$$

σ being the surface tension between the two phases. Q is defined as the flow rate quotient:

$$Q = Q_l/Q_g. \quad (5)$$

For a given value of Re and We we wish to analyze the formation of a stable liquid jet and the dependence of the flow on the quotient Q . In particular, we find out the minimum value of Q , $Q^*(Re, We)$, below which the liquid jet ceases to be stable and a dripping regime is observed in the simulation. The jet is considered to be stable if the liquid meniscus remains steady for a sufficiently large period of time.

We should point out that in order to focus a jet of liquid by gas, moderate-high Reynolds numbers are needed. We consider in detail two different conditions for the focusing gas:

Case 1: $Re = 465.83$, $We = 8.137$.

Case 2: $Re = 931.666$, $We = 32.55$.

Each case will be explored under different flow rate quotients.

A. Numerical procedure

In order to predict the interface geometry during the time-solution, several techniques have been used, falling into one of three categories. These are: (i) interface tracking methods, including a moving mesh, (ii) front tracking and particle tracking schemes, and (iii) interface

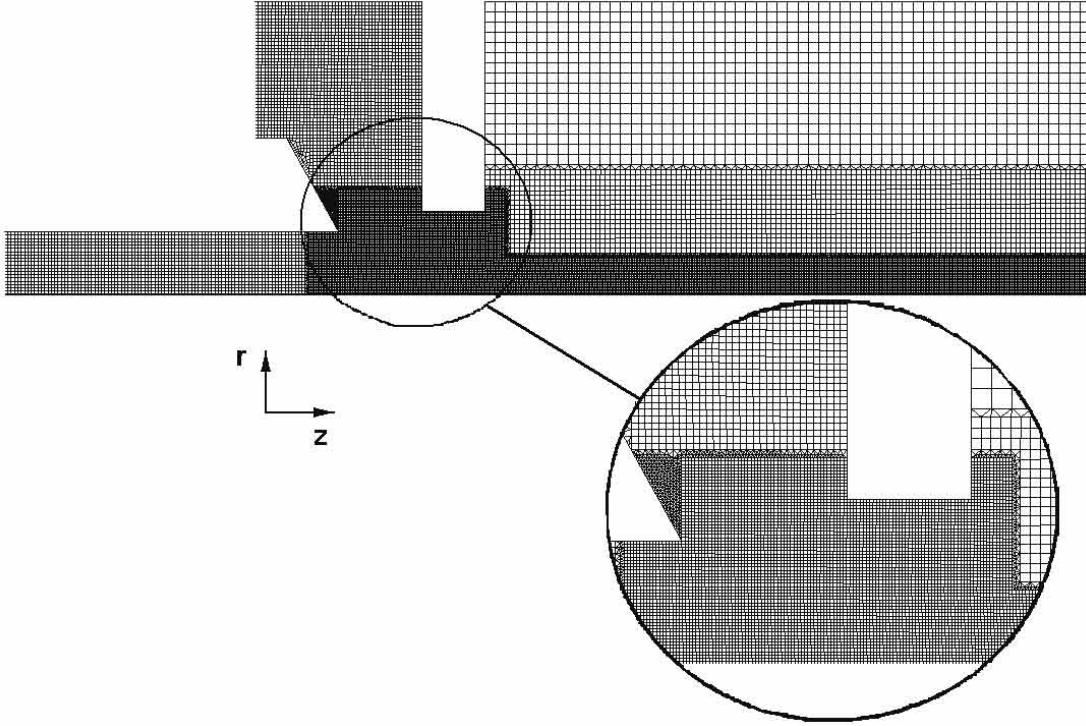


FIG. 2: Grid of the domain under study. A denser mesh is provided in areas where the interface is expected to lie, to avoid the numerical diffusion of the interface, the region where the interface is expected to be located is defined with a higher density of nodes.

capturing methods, including volume of fluid (VoF) and level set techniques. We chose a VoF method consisting of two parts: an interface reconstruction algorithm to approximate the interface from the set of volume fractions and a VoF transport algorithm to determine the volume fraction at the new time level from the velocity field and the reconstructed front.[29] The basic method is robust and flexible, and is based on widely used VoF schemes [30, 31, 32, 33].

We have used a commercial VoF solver (FLUENT, laminar unsteady) to resolve the discretized mass continuity, momentum conservation, and the liquid volumen fraction equations in the mesh depicted in Fig. 2, generated by commercial code GAMBIT. Observe that the smallest quadrilateral elements lie between the needle edge and the nozzle, where the liquid meniscus is located, and in the near-axis region, where we expect the development of the liquid jet. The basic mesh should be sufficiently refined to capture, in the absence of the liquid, the strong velocity gradients experienced by the gas flow at the ori-

face region. In the grid shown in Fig. 2 the minimum cell radial and axial lengths are $(\Delta z)_{min} = (\Delta r)_{min} = 0.02$. Several numerical tests with smaller size mesh cell have shown that this level of accuracy is exceedingly sufficient to describe the gas flow pattern for the two cases considered ($Re = 465.83$ and 931.666). All results presented here were initially computed in that mesh. In all instances where Q was very small, the results were recomputed in a refined mesh with quadrilateral cells in the nozzle and jet region, with $(\Delta z)_{min} = (\Delta r)_{min} = 0.01$. Finally, only for the more difficult cases (case 2 with Q small), the results were recomputed in a finer grid with $(\Delta z)_{min} = (\Delta r)_{min} = 0.005$.

A factor requiring consideration is the location of the outlet boundaries. They are to be sufficiently remote from the nozzle to avoid the numerical reflection of pressure waves, since the pressure is artificially kept fixed at these boundaries during the time evolution of the flow. Moreover, this boundary condition also present problems when the jet goes through the outflow boundary or, worse yet, drops go through it. When a jet extends all the way to the outlet boundary of the flow domain, the pressure in a circular jet and the surrounding fluid cannot be equal due to surface tension. However, for our particular problem and how we will show later, these undesired effects are confined to not more than two diameters upstream of the jet. Therefore, we have carried out the numerical simulations with a external chamber sufficiently large, $z_{out} = 10$ and $r_{out} = 3.5$, to minimize the effects of this BC in the results we present here. On the other hand, the z position where the inlet boundary conditions for the liquid are imposed, has been located sufficiently far away from the needle edge, at $z = z_l = -3$. This choice has been made, as will be shown later, because a liquid recirculation cell intrudes upon the capillary tube when Q decreases. Therefore, in order to impose a Hagen-Poiseuille profile for the liquid velocity as a well posed inlet boundary condition, this boundary should be set sufficiently far upstream from the recirculating region.

Tracking the interface between the phases is accomplished by solving a continuity equation for the volume fraction of one of the phases using an explicit time-marching scheme. The rest of the equations are solved implicitly. The time steps selected were fixed and sufficiently small to ensure that the global Courant number based on the mesh cell size, the mean velocity in the cell and the time step was always smaller than one. Regarding the spatial discretization of the equations, the third-order modified MUSCL scheme[34] is used to obtain the face fluxes whenever a cell is completely immersed in a single phase. When the cell is near the interface, the CICSAM algorithm is used[35]. The pressure corrections are computed

with the body forces weighted scheme and the pressure-velocity coupling in segregated solver is treated with the PISO method [36]. All under-relaxation factors are set to one to avoid any numerical masking of fade-out effects on our physical problem.

III. NUMERICAL RESULTS

We begin by studying the formation of a stable liquid jet in the FF device. Initially, the capillary needle is filled with liquid up to $z = 0$ while the rest of the domain is filled with gas. We start the simulation from rest ($u = v = 0$) in the whole domain except at the inlets, where velocity profiles are prescribed. Fig. 3(a)-3(h) shows the formation of a stable liquid jet for case 1 and $Q = 0.00402$, going through the stages of interface entry, meniscus growth and jet consolidation. The liquid-gas interface is computed in the figure as the iso-level of the liquid volumen fraction $\alpha = 0.999$, obtained with the VOF method. Given that the flow might be unsteady, we consider that the meniscus-jet has reached a stable condition whenever two conditions hold:

1. The angle between the liquid meniscus and the radial coordinate at the capillary needle, $\theta(t)$, has reached a constant value in time, $\theta(t) = \theta_o$.
2. Both the jet diameter at the nozzle inlet, $d_{in}(t)$, and at the nozzle exit, $d_{out}(t)$, should reach a steady regime or a stable oscillating regime around a mean value; these quantities are of course to stay above zero. This amounts to excluding jet breakup in the nozzle region since this implies a non-slender jet: a signal of dripping (v. g. non-stable meniscus-jet).

Here, $d_{in}(t)$ and $d_{out}(t)$ are computed at each time step, by integrating radially the liquid volume fraction, α , at the nozzle inlet, $z = 2$, and at the exit, $z = 2.75$:

$$d_{in}(t) = 2\sqrt{2 \int_0^1 \alpha(t, z = 2, r) r dr}; \quad d_{out}(t) = 2\sqrt{2 \int_0^1 \alpha(t, z = 2.75, r) r dr}. \quad (6)$$

For sufficiently large Q , as illustrated in Fig. 3, both d_{in} and d_{out} evolve towards a steady value.

However, oscillations of these two quantities are observed when Q is reduced. For example, Fig. 4 shows the time oscillation of d_{in} and d_{out} for case 1 and $Q = 0.006$ after allowing

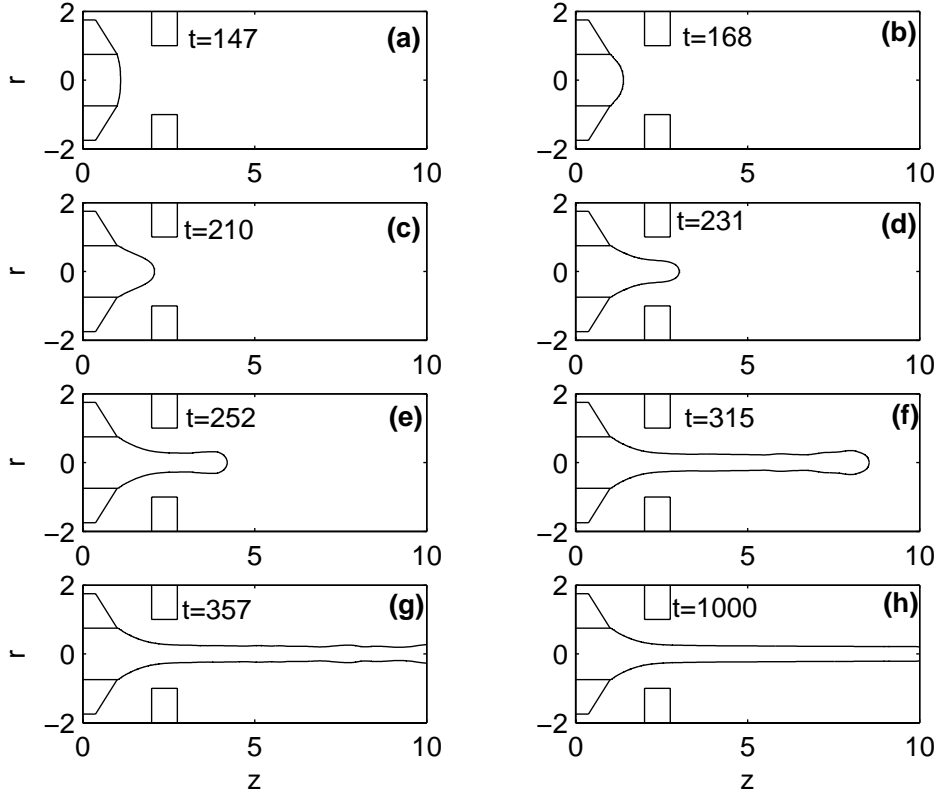


FIG. 3: A sequence of snapshots from the simulated growth of a stable jet (case 1, $Q = 0.004$): (a) the interface arrives to the needle edge; (b)-(c) the meniscus grows in the nozzle region; (d)-(f) a jet begins to issue from the nozzle; (g)-(h) the meniscus-jet system is stable in time.

a stable jet to develop. It can be observed that the jet diameter at the nozzle exit is smaller than at the inlet; mass conservation arguments imply the inlet velocity to be smaller than the outlet velocity (in inverse proportion to the diameter squared). This explains why the oscillation frequencies of the jet diameter are shorter at the outlet. Although the oscillation of the jet in the nozzle region may play an important role in the dynamics of the droplets generated upon jet breakup, our main concern here is to characterize the jet diameter, the angle of the meniscus at the attachment, θ , and the flow structure inside the meniscus as a function of Q . Since the flow is unsteady, we will use a mean value of the jet diameter at the nozzle inlet and outlet as defined by:

$$\bar{d}_{in} = \frac{1}{T} \int_{t_i}^{T+t_i} d_{in}(t) dt, \quad \bar{d}_{out} = \frac{1}{T} \int_{t_i}^{T+t_i} d_{out}(t) dt \quad (7)$$

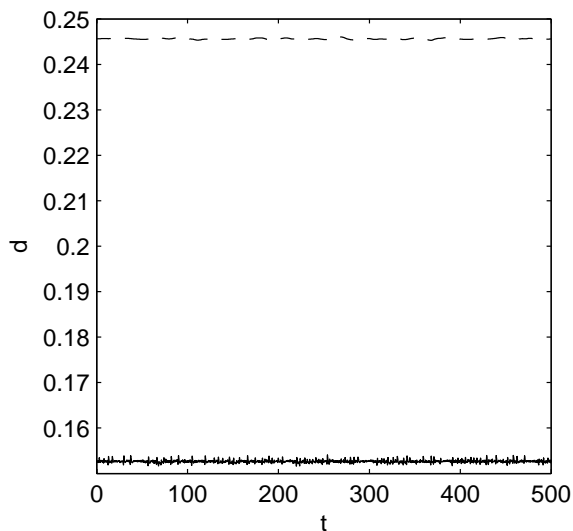


FIG. 4: Time dependence of the jet diameter, d_{in} (up) and d_{out} (down) for case 1 and $Q = 0.0006$. Note the higher frequency in the variation of d_{out} as compared to d_{in} .

where t_i is a time position once a stable jet has developed and T is a time period long enough to ensure a significative mean value. For example, selecting $t_i = 0$ and $T = 500$ leads to $\bar{d}_{in} = 0.2456$ and $\bar{d}_{out} = 0.1527$ (conditions as in Fig. 4).

The procedure is the same for the two gas configurations. The simulation is started from rest with a value of Q sufficiently high to obtain a stable jet. Then, Q is reduced and the solution is monitored in time until a new stable jet is obtained. Fig. 5 shows the stabilized liquid-gas interface for case 1 and different Q . It should be pointed out that $Q = 0.004$ is the smallest flow rate compatible with a stable jet for case 1. Therefore, it can be identified as the minimum flow rate Q^* for stable jetting: $Q^* = 0.004$ for case 1.

Fig. 6 shows the interface for case 2 and different Q values once a stable regime is reached. The smallest jetting flow rate here is $Q^* = 0.001$, four times smaller than in case 1. Accordingly, the smallest jet diameters are obtained for case 2. The jet diameter evolution is shown in Fig. 7, where the mean steady values \bar{d}_{in} and \bar{d}_{out} are plotted as a function of Q for (a) case 1 and (b) case 2. To complete the picture, Fig. 8 shows the dependence of the meniscus angle θ with Q for the two gas configurations. In both cases, θ becomes smaller as Q decreases (smaller flow rate quotient implies stronger focusing action). Just before dripping, as the liquid flow rate is reduced, the angle appears to become independent from Q : the interface geometry becomes invariant (local fluidostatic equilibrium). The smallest angles

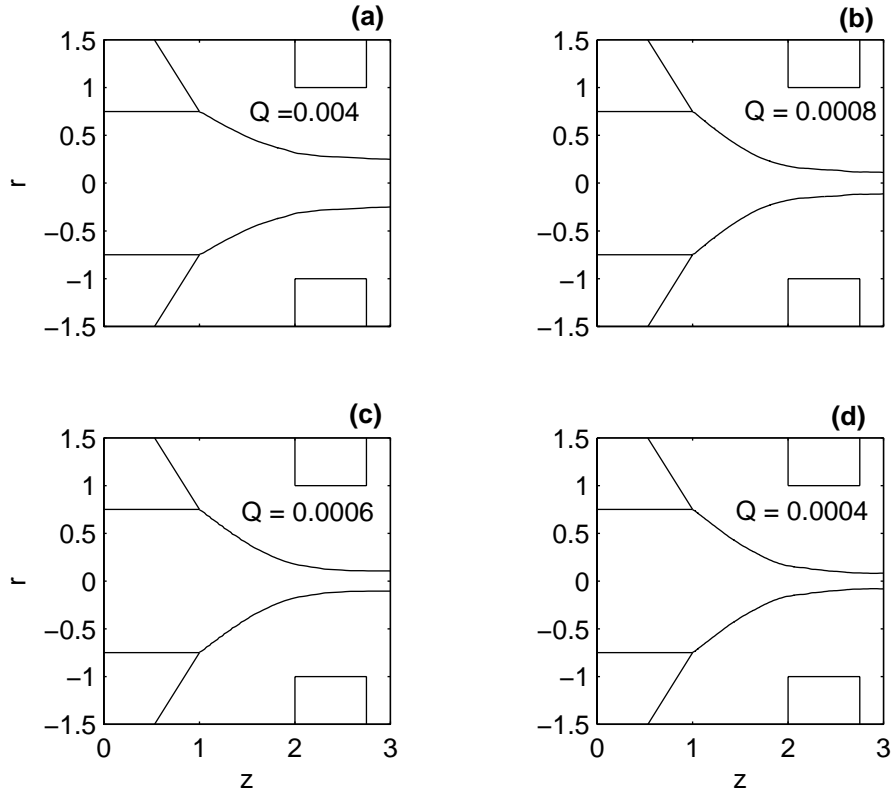


FIG. 5: Variation of the liquid-gas interface as a function of Q (case 1)

are obtained in case 2. This is to be expected since the normal pressure forces produced by the gas stream, which cause the focusing flow, are larger for that case.

Analyzing in more detail the structure of the flow inside the liquid meniscus in jetting mode, in the lower- Q range, a meniscus recirculation cell is observed, in analogy with other co-flowing systems [3, 26] and Taylor cones [24]. Fig. 9 shows instantaneous streamlines for case 1 and different values of Q . The recirculation increases when Q decreases, the cell penetrating into the capillary needle. Fig. 10 depicts instantaneous streamlines for case 2 and four different values of Q . Again, a recirculation region appears before the meniscus jet system ceases to be stable. The size of the recirculation can be calculated by finding the two z -positions where the velocity at the axis becomes zero.

Fig. 11 shows the velocity at the axis, v_{axis} , as a function of z for five different values of Q : (a) case 1 and (b) case 2. It is worth observing that v_{axis} is roughly uniform inside the capillary needle, its value being given by the Hagen-Poiseuille expression; in the nozzle region it increases owing to the focusing effect of the gas stream, which creates the issuing

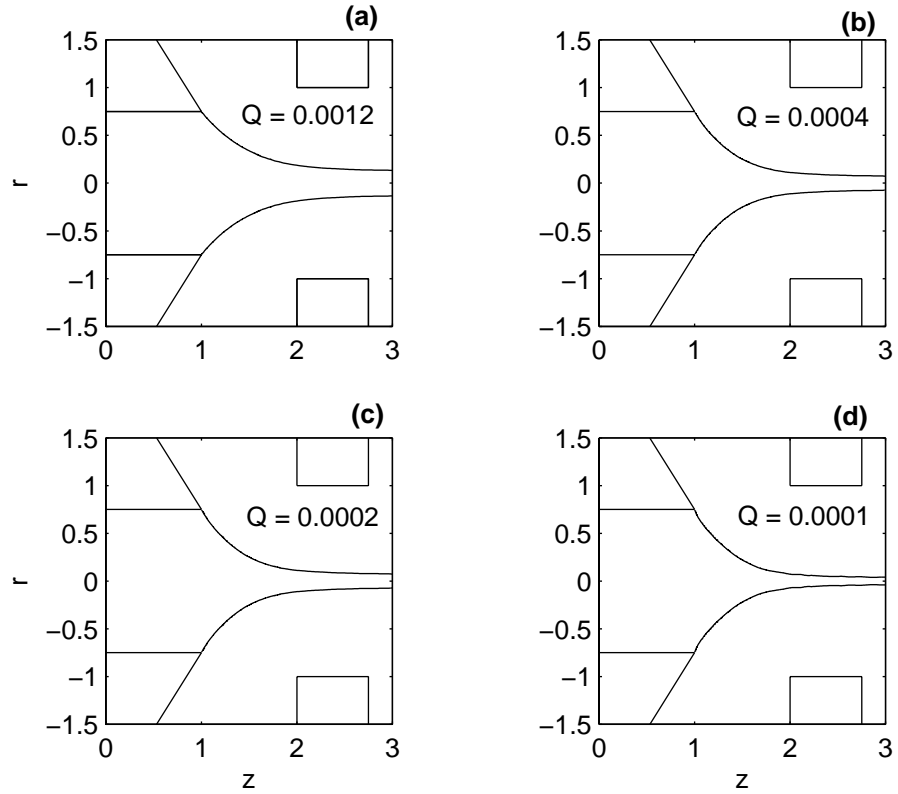


FIG. 6: Variation of the liquid-gas interface as a function of Q (case 1)

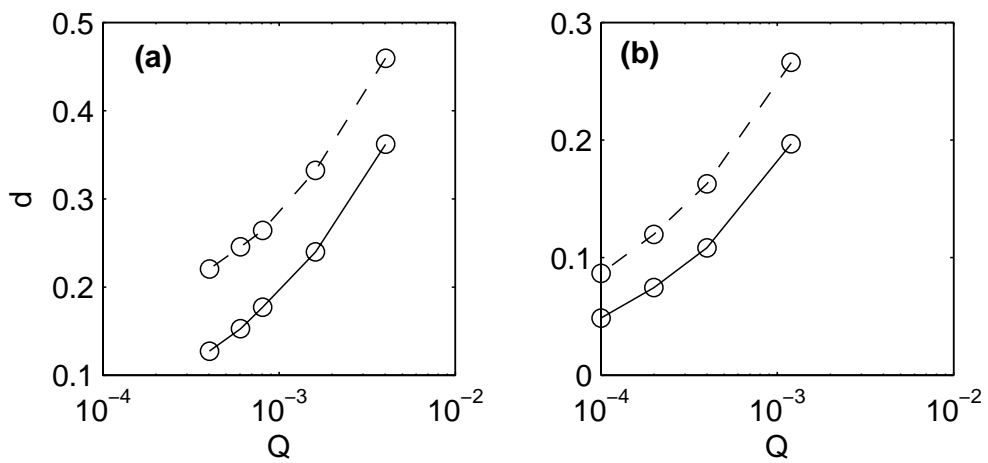


FIG. 7: Mean jet diameter at the inlet (dashed line) and at the exit (solid line) of the nozzle orifice versus the flow rate quotient Q . (a) Case 1, (b) Case 2.

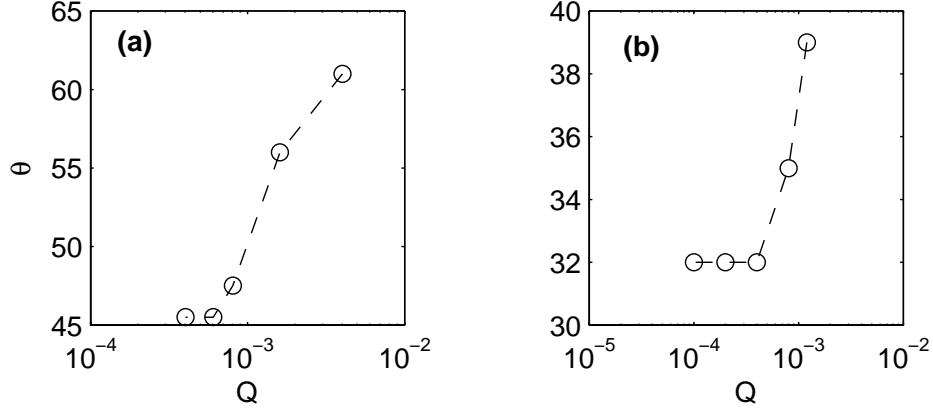


FIG. 8: Angle θ (degrees) versus flow rate quotient Q . (a) Case 1, (b) Case 2.

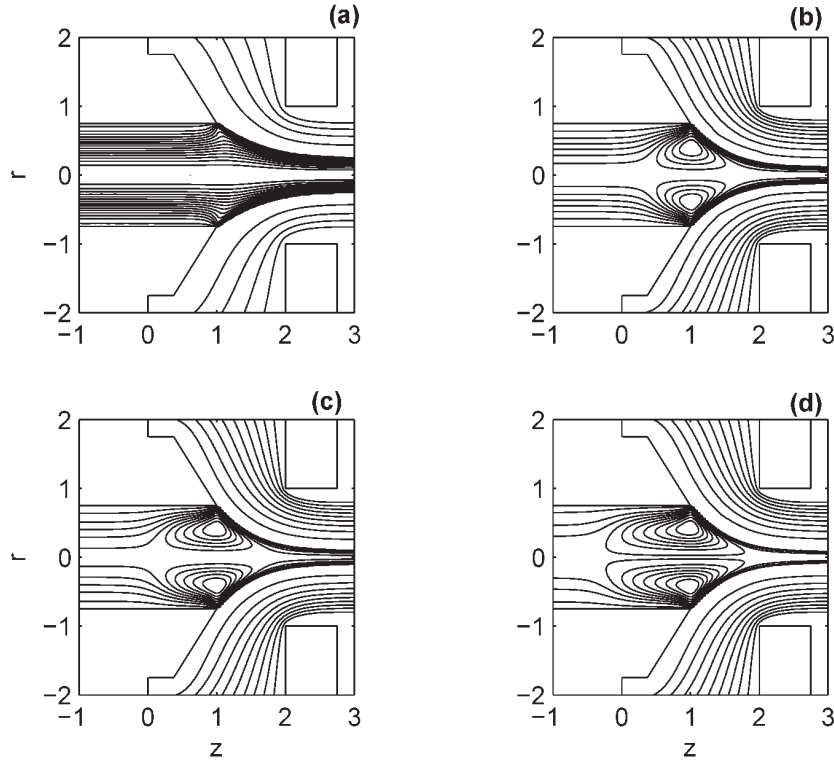


FIG. 9: Instantaneous streamlines at four different flow rates quotients Q for case 1: (a) $Q = 0.004$, (b) $Q = 0.0008$, (c) $Q = 0.0006$ and (d) $Q = 0.0004$.

jet. A region where v_{axis} decreases is located in the meniscus region, between the capillary and the nozzle; note that when Q decreases, a local minimum of v_{axis} is observed at a given position $z = z_{min}$ in the meniscus region. If Q is sufficiently small, v_{axis} becomes negative near the local minimum in a region delimited by the two z positions, z_1 and z_2 , where

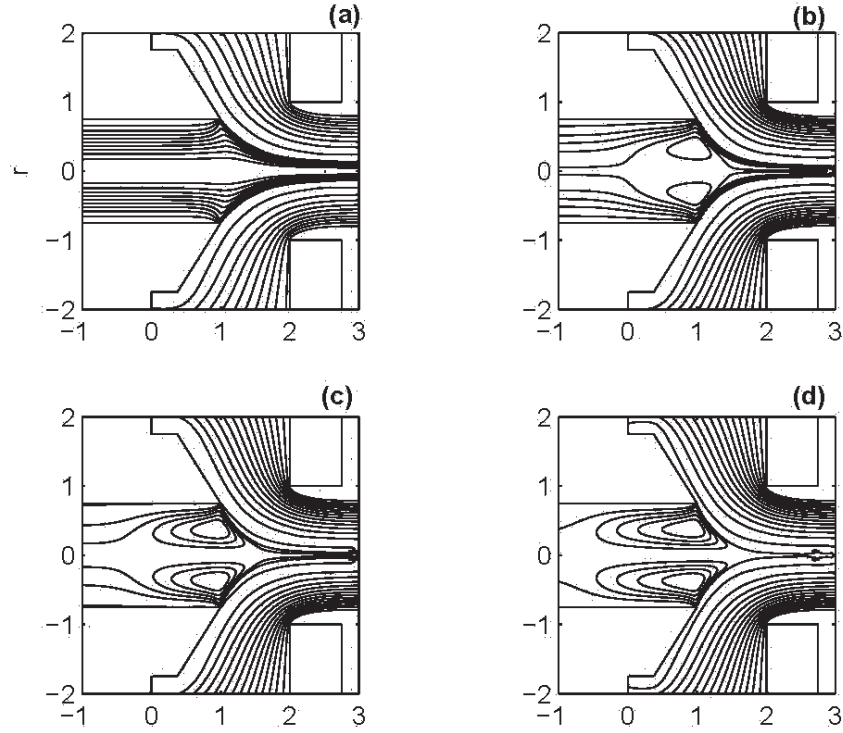


FIG. 10: Instantaneous streamlines of the flow at four different flow rate quotients Q for case 2: (a) $Q = 0.0012$, (b) $Q = 0.0004$, (c) $Q = 0.0002$ and (d) $Q = 0.0001$.

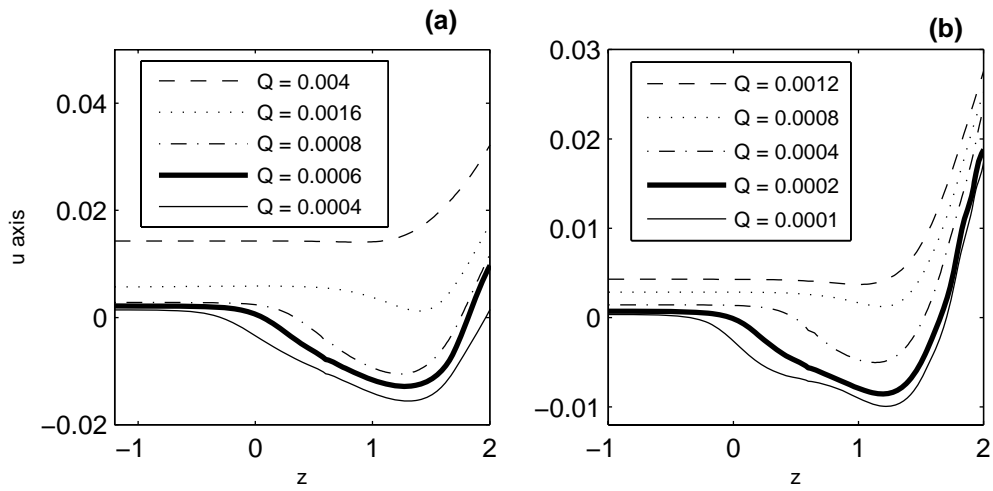


FIG. 11: Velocity at the axis versus z for several flow rate quotients Q : (a) Case 1 and (b) Case 2.

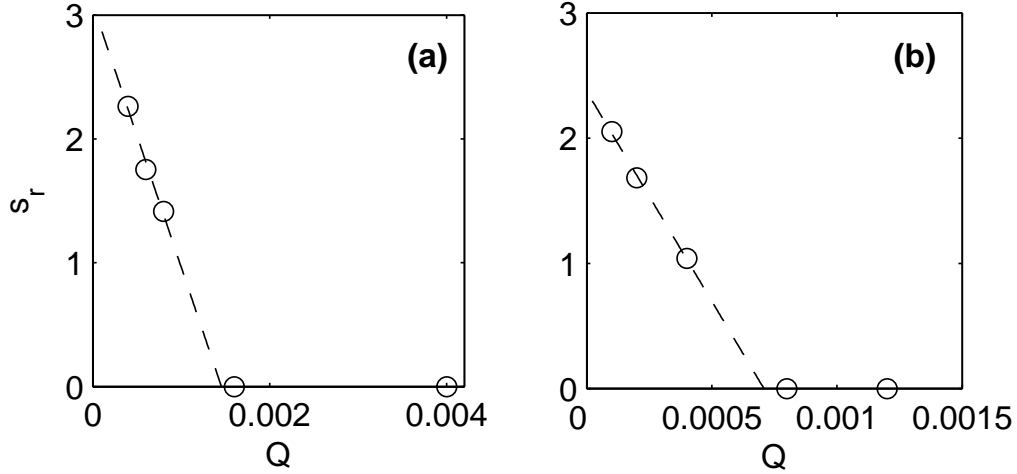


FIG. 12: Size of the recirculation s_r as a function of Q : (a) Case 1 and (b) Case 2.

$v_{axis} = 0$. Therefore, the size of the recirculation region, S_r , observed in Figs. 10 and 11, can be computed as $S_r/R = s_r = z_2 - z_1$. There is a threshold value of Q , Q_r , below which a recirculation pattern is observed. At the threshold flow rate $v_{axis} = 0$ at $z_1 = z_{min} = z_2$ and $v_{axis} > 0$ elsewhere.

Fig. 12 shows s_r as function of Q for (a) case 1 and (b) case 2. Looking back at Fig. 9, note that the size of the recirculation cell increases as Q decreases. In situations of incipient recirculation (Q smaller than but similar to Q_r) this growth appears to be linear, as derived later from dimensional arguments. In Fig. 12, the discrete points 'o' have been obtained directly from the simulations. The dashed lines are linear interpolations computed in the recirculating regime, $s_r > 0$. The linear interpolation is not only in good agreement with the data but also provides a reliable approximation to compute Q_r . The estimations are $Q_r = 0.001453$ for case 1 and $Q_r = 0.000708$ for case 2. According to the above, the linear expression relating the size of the recirculation region and the flow rate Q is:

$$s_r \sim A(Q_r - Q). \quad (8)$$

This means that s_r is proportional to a *back flow* rate $Q_B/Q_g = Q_b = (Q_r - Q)$ for a given set of fluid properties, geometry, and gas flow Reynolds number. The relative location of the jetting threshold Q^* and the recirculation threshold Q_r is, in both cases, $Q^* < Q_r$. This implies that recirculation can be taken as a dripping-precursor: as far as can be gathered from our simulation, it always precedes global instability of the meniscus-jet system.

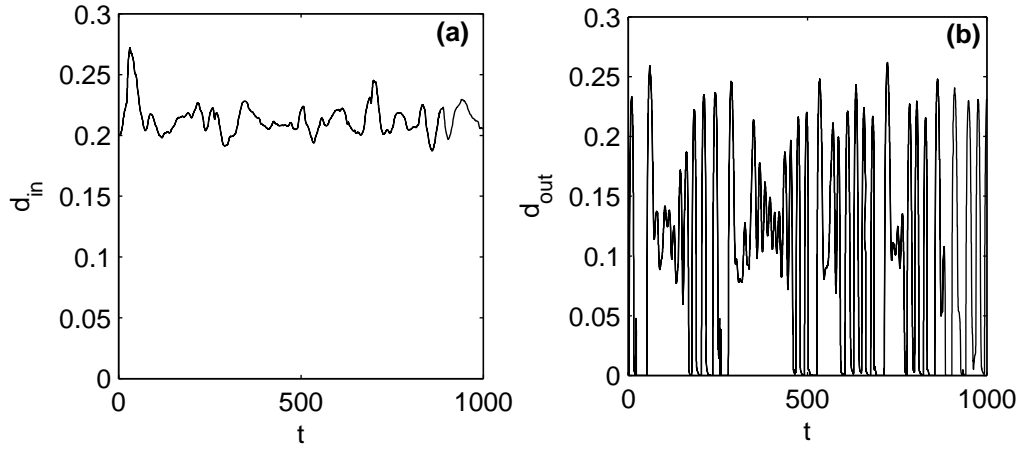


FIG. 13: Time evolution of (a) d_{in} and (b) d_{out} in a irregular dripping regime for case 1 and $Q = 0.000322$.

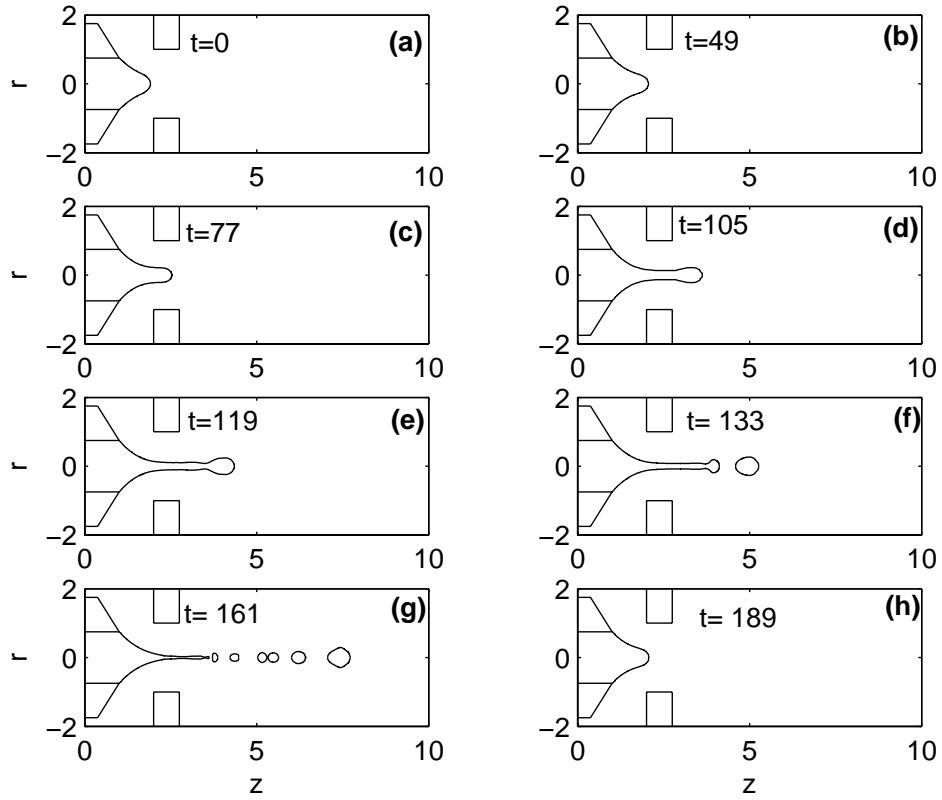


FIG. 14: A sequence of the dripping regime for case 1 and $Q = 0.000241$ involving a complete cycle.

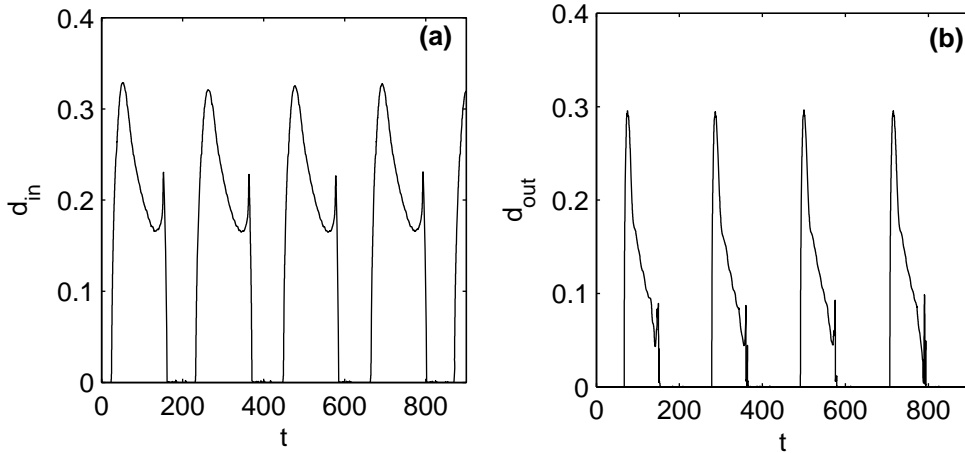


FIG. 15: Time evolution of (a) d_{in} and (b) d_{in} in a dripping regime for case 1 and $Q = 0.000241$.

Finally, some results are presented with flow rate values below the jetting threshold. For $Q < Q^*$, with Q close to Q^* , our simulations show the flow to exhibit different behaviors in a sequence: a period where a thin jet breaks up in the nozzle region alternates with other periods where a thin jet breaks up downstream of the nozzle. The irregular time behavior of the flow for $Q < Q^*$, but Q close to Q^* (*incipient dripping*) can be observed in Fig. 13, where d_i (a) and d_{out} (b) are shown as a function of time for case 1 and $Q = 0.000322$. For $Q < Q^*$ but Q sufficiently different from Q^* , the flow behavior becomes more regular and periodic with a unique dripping frequency. A detailed study on an analogous problem for a dripping faucet was performed by Coulet, Mahadevan and Riera.[37] Here, some cases of fully developed dripping have been studied in detail. Fig. 14 shows a complete time sequence of a regular dripping process (case 1, $Q = 0.000241$). Subfigures (a)-(e) show the growth of the meniscus and the formation of a jet issuing from the nozzle; subfigures (g)-(h) show the jet breakup into droplets of different sizes and the meniscus recoil. This is a periodic sequence, the period being $T \sim 210$ for each cycle. Fig. 15 plots d_i (a) and d_{out} (b) as a function of time for this case. Initially, a liquid meniscus is growing with no jet production, and $d_{in} = d_{out} = 0$. Subsequently, a liquid jet issues and d_{in} and d_{out} become positive. Both

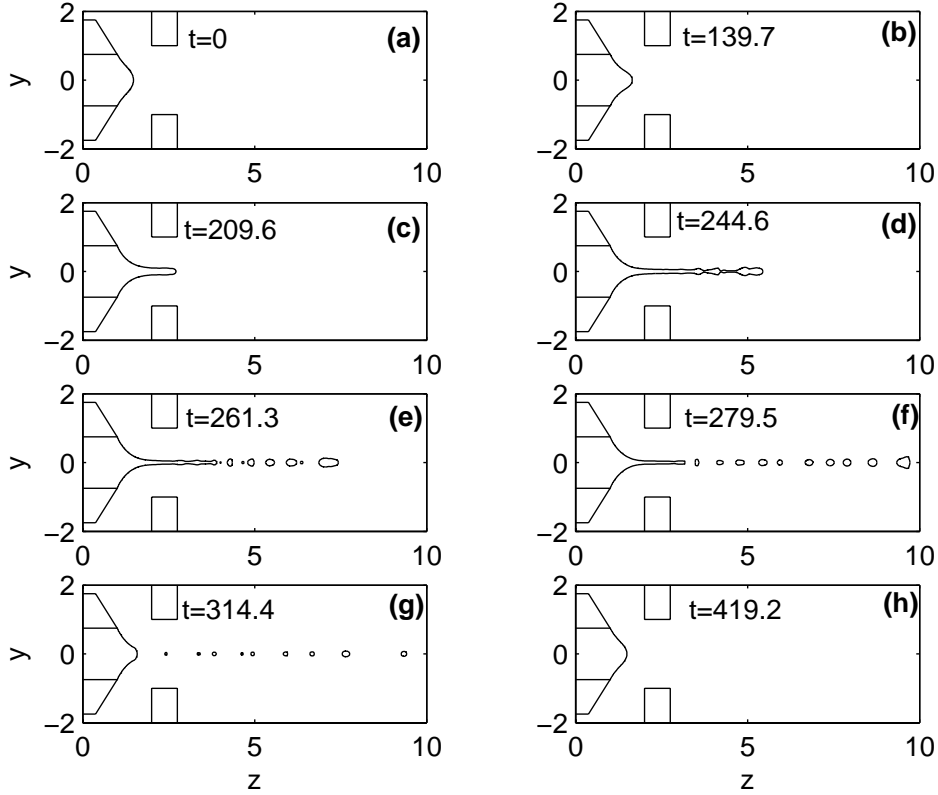


FIG. 16: A sequence of the dripping regime for case 2 and $Q = 0.00004$ involving a complete cycle.

diameters reach a maximum at a certain time and then start to decrease. Finally, the jet breaks into droplets, d_{in} and d_{out} are set to zero and the process begins anew. The dripping process in this case is quite similar to regular faucet dripping, the time period being mainly imposed by the filling of the meniscus until reaching a critical volume.

A similar situation is observed in case 2. Fig. 16 shows a complete time sequence of a regular dripping process with $Q = 0.00004$. Subfigures (a)-(d) show the meniscus growth and the emission of a jet, much thicker and longer than observed in Fig. 14. Again, this sequence is time periodic with a period $T \sim 500$ for each cycle (see d_i (a) and d_{out} (b) in Fig. 17 as a function of time).

1. Influence of the BCs and the spatial and temporal resolution on the numerical results

The numerical problem we are trying to solve is quite complex since we have a high speed stream of gas discharging through a nozzle into a infinity large chamber plus a meniscus-

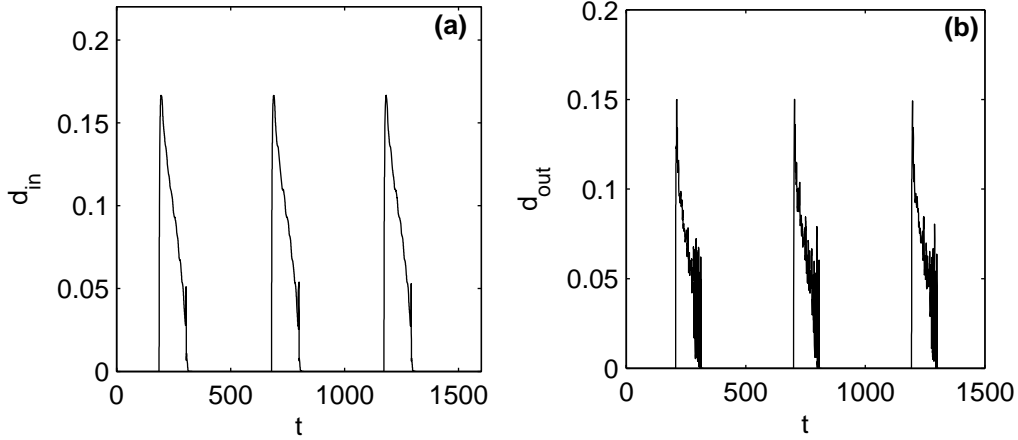


FIG. 17: Time evolution of (a) d_{in} and (b) d_{in} in a dripping regime for case 2 and $Q = 0.00004$

liquid jet which may break into droplets inside our finite numerical domain. This complexity yields to the existence of different time and spacial scales associate to different physical phenomenons involved in the problem (jet breaking due to capillary and Kelvin-Helmholtz instabilities, mixing layer instabilities in the main gas steam and interaction between these two phenomenons), and it makes the accurate analysis of the jet breaking quite hard to archive. These are the reasons for which, although our VOF method qualitatively predict the breaking of the jet and the drop formation, we have focus our attention in this subsection to ensure the independence of our numerical results (meniscus-jet shape as a function of Q for different gas configurations) on the selected BCs and numerical meshes.

As we have told in the numerical procedure, the more problematic BC is the election of $p = 0$ at the outlet boundaries, since any jet or a drop passing trough that boundary is affected by the strong restriction that the pressure is kept fixed. However, let us demonstrate that by putting the external boundary sufficiently away from the nozzle region, at $z_{out} = 10$, the meniscus-jet is not affected by that numerical condition. To show this, we have considered the worse escenario, which is archived, by selecting the larger values of the liquid flow rate (Q large) and the less strong gas configuration (case 1). Fig. 18 shows the stabilized

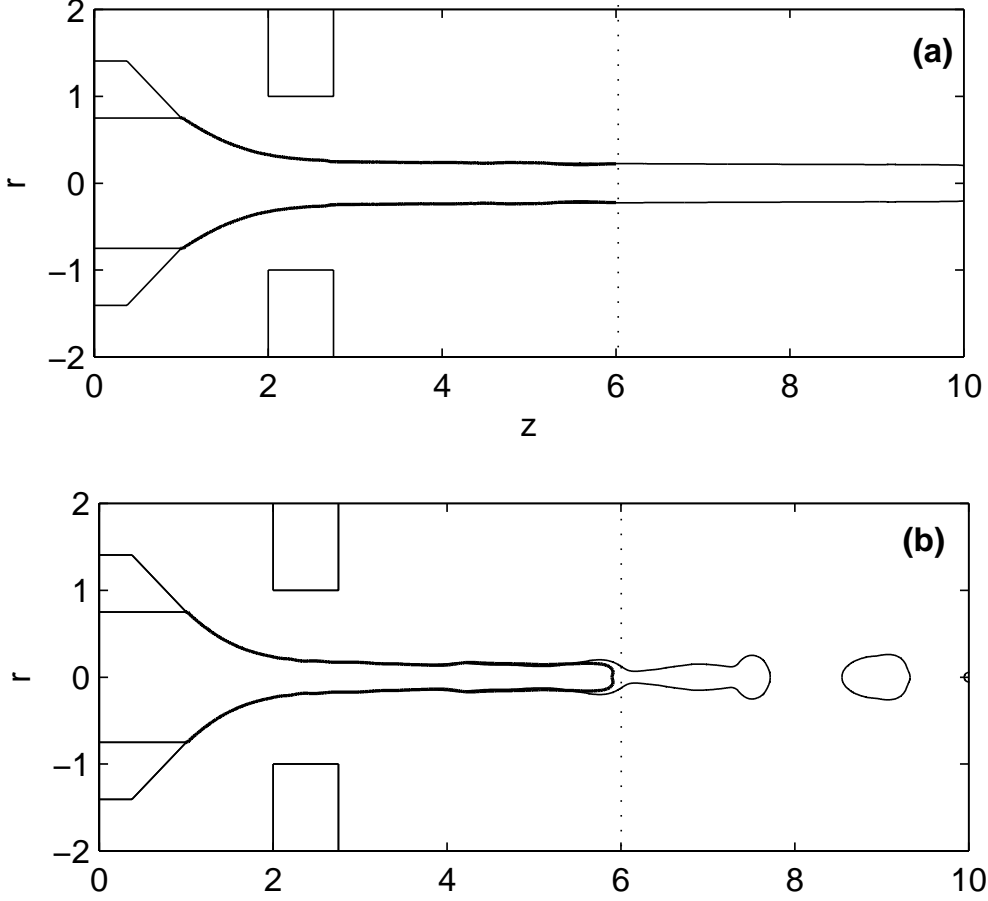


FIG. 18: The effect of the $p = 0$ boundary condition on the liquid-gas interface when this condition is applied at $z = 6$ (thicker line) instead of at $z = 10$ (thinner line):(a) corresponds to case 1 and $Q = 0.004$; (b) corresponds to case 1 and $Q = 0.0008$.

liquid-gas interface for case 1 and two different value of Q , computed in the original domain and in a shorter one. In Fig. 18(a), the jet does not break inside any of the two numerical domains and it can be seen that the interface meniscus-jet in the nozzle region is not affected by the imposed $p = 0$, boundary condition. In fact, the jet is just affected a few diameters upstream of the boundary. In the case considered in Fig. 18(b), the jet is breaking into drops inside the large domain. Even in this case, the interface meniscus jet in the nozzle region is not affected by the artificial boundary condition.

Let us now to show the consistency of the results by comparing the results in two different

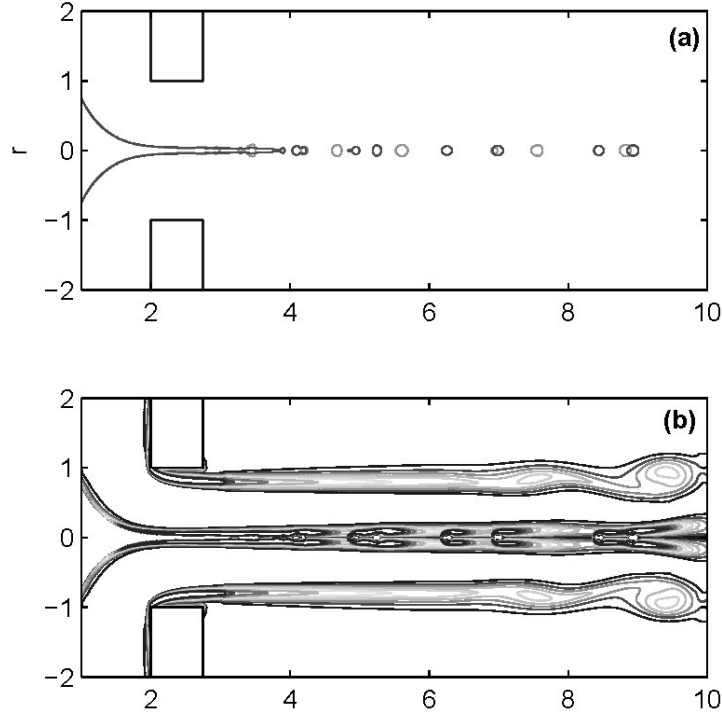


FIG. 19: The effect on the liquid-gas interface of changing the spatial resolution : (a) shows a general view of case 2, $Q = 0.0001$ where the grey line corresponds to the solution computed in mesh with $(\Delta_z)_{min} = (\Delta_r)_{min} = 0.01$ and the black line is the solution obtained in a mesh with $(\Delta_z)_{min} = (\Delta_r)_{min} = 0.005$.; (b) shows contours of the vorticity field for this same case with the best spatial resolution.

meshes. In this case again, we have considered the worse scenario, which is archived, by selecting the smaller values of the liquid flow rate (Q small) and the stronger gas configuration (case 2) since thinner jets are obtained in these cases. Fig. 19 (a) shows a instantaneous picture of a stable liquid jet breaking into drops for case 1 and $Q = 0.0001$ computed in two different meshes. Observe that although we are comparing the liquid interface at two different times and with different spatial resolution, the shape of the meniscus of the liquid in the nozzle zone is the same for the two cases. The main difference is that the liquid jet it is a little be longer in the fined mesh. As we have mentioned, the accurate description of the jet breaking, which is not the objective of this work, is hard to ensure due to the different physical phenomenon involved. To show this, in figure 19 (a), where we are despited instantaneous contours of the vorticity field for this case, computed with the best spatial

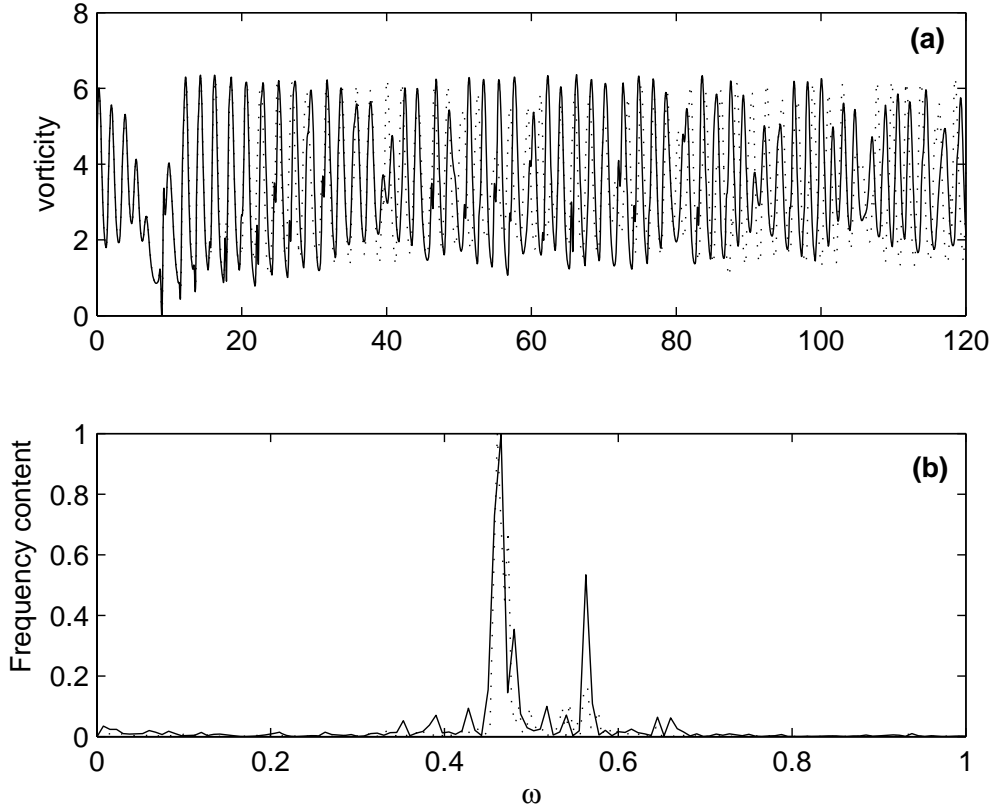


FIG. 20: a) Comparison of the time evolution of the vorticity magnitude at the point ($z = 9.5$, $r = 0.995$) for case 2 and $Q = 0.0001$ computed with $\Delta t = 0.014$ (solid line) and with $\Delta t = 0.028$ (dashed line); b) shows the comparison in frequencies of the two signals.

resolution. It can be seen, that due to the large value the large differences of density and velocity between the liquid and the gas, the vorticity is large in the liquid-gas boundary layer which is developing over the liquid-jet meniscus. When the jet breaks we can also see that the behavior of the flow around the drops is similar to the flow at high Reynolds numbers over a round object (since the gas is traveling faster than the liquid drops). Therefore, we also have boundary layer separation over the surface of the drops and the formation of the wake downstream of the drop. In addition to this, a mixing layer is developing downstream of the nozzle edge due to the differences between the velocity of the gas flowing through the nozzle and the outside stagnation atmosphere. This mixing layer yields to the development of vortices like the one which can be seen in the figure. Figure 20(a) shows the time evolution of the vorticity magnitude at a point of this mixing layer computed with two different

time steps. It can be seen the strong fluctuations of the vorticity magnitude. Although, some differences in the time evolution becomes appreciable when time increases, both time resolutions are enough to predict the characteristic frequencies of the problem at the point of observation. In effect, Figure 20(b) show the frequency content of the magnitude of the vorticity obtained by applying the Fast Fourier transform (FFT) two the two signals. The main frequency $\omega_1 \sim 0.46$ is related to the pass of the vortices generate in the gas mixing layer. There is also another characteristic frequency, $\omega_2 \sim 0.56$, which is associated to the interaction between the mixing lager and the vorticity wake of the drops. We arrived to this conclusion after recomputing the flow without the liquid jet, where in the frequency content of the magnitude of signal at the same point of observation only the frequency $\omega_1 \sim 0.46$ remained as the more important one.

IV. COMPARISON WITH ANALYTICAL MODELS AND SCALING LAWS

The first predictive model for the jet diameter d_j at the orifice exit [6] assumes that viscous and capillary effects are small enough compared to liquid inertia. This demands large enough Reynolds and Weber numbers of the liquid jet, in reasonable agreement with most experimental conditions (common solvents including water, down to the micron scale). In this limit, the overall pressure difference $\Delta P = \Delta P(Q_g)$ imposed in the downstream direction (i.e. through the orifice), transmitted to the liquid stream by normal surface stresses, is converted into kinetic energy, such that

$$\Delta P \simeq \frac{1}{2}\rho_l v^2 \simeq \frac{8Q_l^2}{\pi^2 d_j^4}, \quad (9)$$

which readily gives

$$d_j = \left(\frac{8\rho_l}{\pi^2 \Delta P} \right)^{1/4} Q_l^{1/2}. \quad (10)$$

Furthermore, the jet is assumed sufficiently small compared to the orifice diameter D such that no only it does not touch the orifice borders, but also the boundary layers of the focusing fluid (gas) at the orifice and at the jet's surface are sufficiently small compared to the corona defined between the jet and the orifice. This is why D does not enter expression (10).

Interestingly, if one neglects viscous effects, surface tension, and one assumes $d_j \ll D$, the only operating parameters left in the analysis are $\{\rho_l, \Delta P, Q_l\}$; using these three parameters, a scaling law identical to 10 -regardless the constants- follows from dimensional

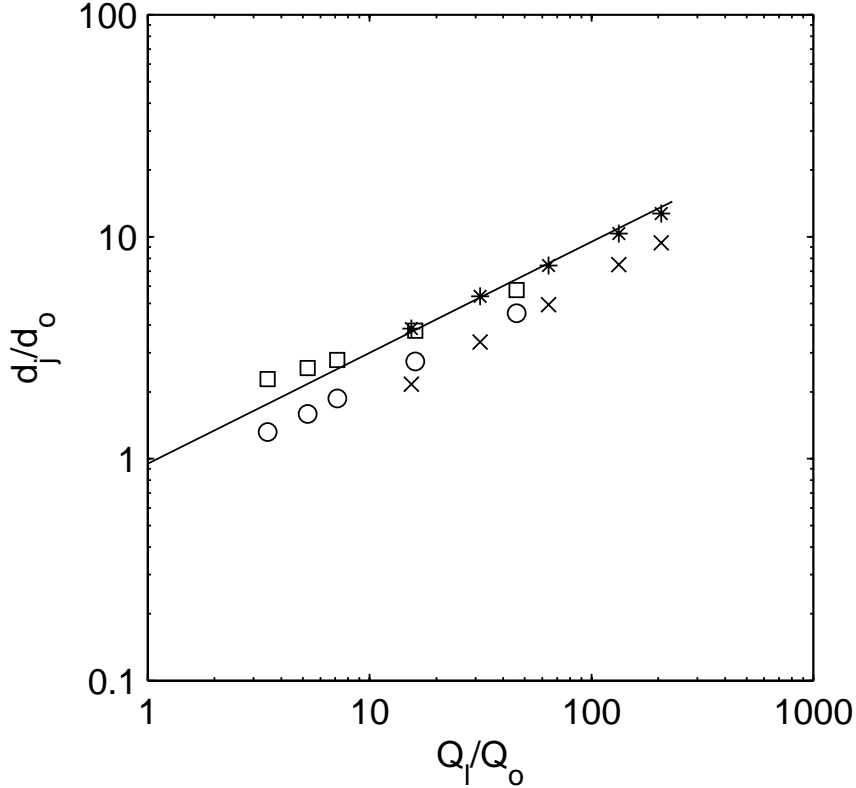


FIG. 21: Jet sizes measured at the entrance of the nozzle using \bar{d}_{in} (\square correspond to case 1 and $*$ to case 2) and at the exit using \bar{d}_{out} (o correspond to case 1 and \times to case 2) compared to the theoretical prediction (continuous line).

reasoning. Figure 21 illustrates the accuracy of this first simple prediction. However, that expression does not provide information on *how small* the neglected effects are. Would it be possible to quantify *both* the dependence of the jet diameter on the three main parameters and the relative magnitude of each one of the neglected effects? The answer is yes, naturally, by retaining either σ , μ_l , or D in the dimensional analysis, and using $\{\Delta P, \sigma, \rho_l\}$, $\{\Delta P, \mu_l, \rho_l\}$ or $\{\Delta P, D, \rho_l\}$ as independent parameters, respectively.

In physical terms, the relative effect of surface tension may be determined by observing that the liquid Weber number must be of order unity ($We_l = \rho_l 8Q_l^2 / (\pi^2 \sigma d_j^3)$) for a given pressure ΔP , from which one obtains the limiting diameter d_o and flow rate Q_o . The result is $d_o = \sigma / \Delta P$ and $Q_o = (\sigma^4 \rho_l^{-1} \Delta P^{-3})^{1/2}$, so that dimensional analysis together with equation (10) readily yields

$$d_j/d_o = k_d(Q_l/Q_o)^{1/2} \quad (11)$$

where $k_d = (8/\pi^2)^{1/4}$. This expression provides a first-order approximation to the jet diameter (asymptotically true for $Re \rightarrow \infty$) as far as $d_j \gg d_o$ (negligible surface tension). The ratio Q_l/Q_o spans the whole domain from jetting to dripping -where d_j becomes comparable to d_o -. Jet diameters and flow rates comparable to d_o and Q_o , respectively, lead to absolute instability, where the characteristic velocity of upstream capillary waves $O(\sigma\rho_l^{-1}d_j^{-1})^{1/2}$ -a product of surface tension- becomes of the order of the downstream convective velocity, Q_l/d_j^2 . Besides, Eq. (11) is explicitly independent of the orifice diameter D , an illustration of the jetting regime independently of its forcing geometry.

Similarly, viscous effects can be weighted by defining a viscosity-related length $d_\mu = (\mu_l^2\rho_l^{-1}\Delta P^{-1})^{1/2}$ and flow rate $Q_\mu = (\mu_l^4\rho_l^{-3}\Delta P^{-1})^{1/2}$. Using these and equation (10), an entirely analogous expression is obtained in the limit of dominant inertia, i. e. when $d_j \gg d_\mu$ and $Q_l \gg Q_\mu$:

$$d_j/d_\mu = k_d(Q_l/Q_\mu)^{1/2}. \quad (12)$$

This equation expresses the jet diameter as compared to a limit where viscous effects become important. Again, jet diameters and flow rates comparable to d_μ and Q_μ , respectively, amount to non-negligible viscous effects and significant departures from predictions (11) or (12).

A third expression can be obtained in terms of the orifice diameter D , and the maximum liquid flow rate that can be ejected through the orifice for a given ΔP in the absence of viscous effects: $Q_{max} = (\pi^2/8)^{1/2}Q_m$, where -naturally- $Q_m = (D^4\Delta P\rho_l^{-1})^{1/2}$ is obtained from dimensional analysis using $\{\Delta P, D, \sigma\}$. Using (10) anew, one has:

$$d_j/D = (Q_l/Q_{max})^{1/2} = k_d(Q_l/Q_m)^{1/2}. \quad (13)$$

This alternative expression reflects how close the experiment is from a situation where the entire orifice section is filled with liquid: it provides information -from continuity arguments- on the fraction of the orifice cross section occupied by the liquid jet.

Each of the above three expressions (11), (12) and (13) amount to interesting but partial pictures of the particular working conditions of our system in a given flow situation. Taken as a whole, they provide a more complete picture on the FF jetting conditions. Some corrections can be obtained for several neglected effects.[16]

2. *Correction for surface tension effects*

The liquid surface tension reduces the effective pressure drop ΔP_l in the liquid stream as

$$\Delta P_l = \Delta P - 2\sigma/d_j. \quad (14)$$

Consequently, the jet velocity decreases and its diameter increases accordingly. The resulting expression for the non-dimensional jet diameter d_j/d_o , neglecting third order terms proportional to $O(d_o/d_j) \ll 1$, reads:

$$d_j/d_o = (8/\pi^2)^{1/4}(Q_l/Q_o)^{1/2} + 1/2. \quad (15)$$

In other words, the second order correction of the jet diameter d_j to account for surface tension effects is asymptotically equal to $d_o/2$.

3. *Correction for liquid viscosity effects (extensional stresses)*

Assuming that the extensional viscous forces in the liquid are smaller than inertia, the balance of the different terms of the momentum equation, including the second order terms of the expansion, leads to the following order of magnitude for the correction to the first order diameter (10):

$$d_e = O \left[d_\mu \left(\frac{Q_{max}}{Q_l} \right)^{1/2} \right] \quad (16)$$

4. *Correction for tangential stresses owing to the gas stream*

In the same way, the diameter correction (decrease) owing to the momentum injected by the much faster gas stream through the jet surface is of the order of:

$$d_g = O \left(\frac{\mu_g U_g D}{\Delta P} \right)^{1/2} \quad (17)$$

where μ_g and U_g are the gas viscosity and velocity. The latter is of the order of $U_g \sim O(\Delta P/\rho_g)^{1/2}$, where ρ_g is the gas density.

The relative weight of these three corrections provides information on the importance of the surface tension and the viscosity of the liquid and gas phases. Interestingly, for most common solvents, these relative weights are of order unity. This happens to be the case

when measuring the relative importance of the surface tension and the gas tangential stress effects for water focused by any gas at standard conditions. Therefore, since both corrections are opposite, the best agreement with experimentally measured jet diameters and numerical simulations is obtained, interestingly enough, using the first order expression (10), or its alternative forms (11-13).

5. Correction owing to the nozzle flow pattern

The jet diameter as measured at the nozzle may also differ from the simplest theoretical prediction given by Eq. (10) because of local flow effects. A complex but symmetric structure develops owing to the coexistence of (i) a core potential flow and (ii) the detachment of a radially convergent boundary layer at the inner lip of the nozzle. In any real situation where the gas viscosity is *non-zero* and the continuum hypothesis holds, this flow pattern is not aptly described by the pure potential flow through a round orifice given by Morse and Feshback[38] (page 1294) for a stationary discharge. The potential flow solution is characterized by an axial velocity distribution with a minimum value at the axis, $v(r = 0) = 2Q_g/(\pi D^2)$ (half the average velocity through the orifice), and an infinite value at $r = D/2$, Q_g being the theoretical gas flow rate discharged. The actual flow geometry is characterized by the well known *vena contracta* effect, a consequence of the radial momentum carried by the collapsing potential flow, which slips at the nozzle border owing to the boundary layer. The *vena contracta* flow exhibits an axial velocity distribution which echoes the potential flow solution, showing a local minimum velocity at the axis, and a maximum value at the streamlines coming just from the outside of the boundary layer detached at the orifice (see Fig. 9). The immediate consequence of this particular flow structure is that the transversal pressure gradients are negligible only sufficiently far downstream of the inner lip of the nozzle: in fact, they become negligible at the axial downstream station where the *vena contracta* effect ends, i.e. where the streamlines become almost parallel. It occurs relatively close to the inner orifice plane, at an approximate $D/2$ downstream distance. From this point downstream (before shear instabilities of the gas stream with the external environment develop), the gas pressure can be considered almost constant, equal to the outside stagnation value. It is at this point where the liquid jet diameter obtained from the numerical simulation should be compared to the simplest prediction (10).

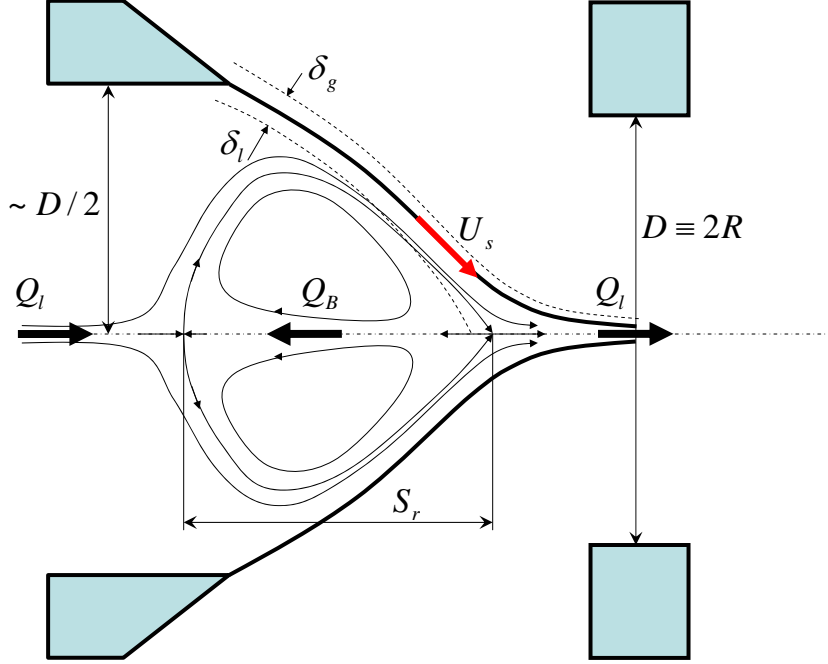


FIG. 22: Sketch of the recirculation zone, showing boundary layers, cell size (S_r), and typical velocities.

A. Scaling of the recirculation zone

For a given gas flow rate Q_g and orifice diameter $D = 2R$, the typical gas velocity close to the meniscus surface can be estimated as $V = Q_g/(\pi R^2)$. Given the small $\rho = \rho_g/\rho_l$ values in liquid jets focused by gas, liquid velocities are much smaller than V everywhere. As the liquid approaches the neck, the boundary layer will collapse (Fig. 22). This implies that at least a liquid flow rate

$$Q_R \sim U_s \delta_1^2 \quad (18)$$

would be drawn into the jet in the absence of recirculation. On the contrary, whenever $Q_l < Q_R$, part of Q_R must have been recirculated back into the meniscus (Fig. 22). Therefore Q_R can be interpreted as the minimum flow rate for no recirculation (scaled as $Q_r = Q_R/Q_g$).

The boundary layer in the liquid meniscus is confined and its growth is limited by the

size of the area where gas speed gradients are steep, of the order of R :

$$\delta_l \sim (\mu_l R / \rho_l U_s)^{1/2}. \quad (19)$$

Whenever there is recirculation, the peripheral boundary layers merge at the meniscus apex and give rise to a jet, whose initial radius at the neck will accordingly be of the same order:

$$\frac{\delta_l}{R} \sim \frac{\mu_l}{\rho_l U_s R} \quad (20)$$

In the absence of liquid emission, maximum recirculation will be observed. Experimentally, however, a dripping instability will occur before reaching this limit. In the opposite case (no recirculation), the boundary layers do not merge, and an inviscid core should be observed at the neck. Interestingly, the threshold flow rate for recirculation, Q_R , results independent of the gas velocity:

$$Q_R \sim R \frac{\mu_l}{\rho_l} \implies Q_r \sim \frac{\rho}{\mu Re} \quad (21)$$

This scaling is fully confirmed by the numerical simulations: the values of $Q_r \cdot Re$ are 0.6768 for case 1 and 0.6596 for case 2, deviating by less than 2.6% from the scaling predictions.

Assume now the recirculation cell to be S_r in axial length. The backflow $Q_B = Q_R - Q_l$ will come to rest within a length of the order S_r . In this length, viscous momentum diffusion will slow down the flow and deflect both the incoming flow injected by the feeding tube and the recirculated flow at the axis (Fig. 22). Thus, viscous and inertia forces should balance within that length S_r : in other words, the liquid Reynolds number associated to axial lengths of order S_r should be of order unity so as to deflect the unidirectional flow issuing from the feed tube (Hagen-Poiseuille). This is in analogy to the entry length or exit length in laminar pipe flow. Two cases need to be considered, depending of the relative size of the cell compared to the feed tube radius R_1 :

- When $S_r < R_1$, viscous stresses, of the order $O(\mu_l Q_B S_r^{-3})$, should balance inertia, $O(\rho_l Q_B^2 S_r^{-4})$, which leads to $S_r \sim \rho_l Q_B \mu_l^{-1}$.
- When $S_r > R_1$, viscous forces, $O(\mu_l Q_B R_1^{-4})$, should balance inertia forces, $O(\rho_l Q_B^2 R_1^{-4} S_r^{-1})$, leading again to $S_r \sim \rho_l Q_B \mu_l^{-1}$.

Interestingly enough, again, the length of the recirculation flow is independent of the gas flow for any given geometry. The latter scaling can be expressed in non-dimensional terms

as:

$$s_r \equiv S_r/R \sim \mu_l(Q_R - Q_l)\rho_l^{-1}R^{-1}. \quad (22)$$

Using equation (18), one may write:

$$s_r = C_1 - C_2 Re_R, \quad (23)$$

where $Re_R = \rho_l Q_l / (\mu_l R)$ is a Reynolds number of the liquid flow, and C_1 and C_2 are constants which depend on the geometry only (i.e., R_1/R , H/R , etc.). In our case, we have represented all our measured s_r values from numerical simulations versus Re_R in Fig. (23). Linear fitting to all points leads to $C_1 = 2.636$ and $C_2 = 0.0819$ with a correlation coefficient of 94.4%. Equation (23) can be expressed in terms of $Q_r - Q$ and Re as well, as:

$$s_r = k\mu\rho^{-1}(Q_r - Q), \quad (24)$$

where k is again a constant depending on the geometry only, in full agreement with expression (8), as anticipated by experiments.

V. EXPERIMENTAL

In the following, we provide experiments corresponding to the same local geometrical parameters as in cases 1 and 2 in the vicinity of the exit orifice. The basic flow focusing chamber is a box consisting of five aluminum faces and one clear methacrylate face. It is 5 cm by 5 cm by 5.65 cm, with its longest side along the capillary/orifice axis. The chamber is situated with the methacrylate face of the cube pointing upwards and the capillary parallel to table-top. The orifice is made in a stainless steel orifice disk attached to the box side perpendicular and opposite to the capillary. The disk is 4.0 mm in diameter with a thickness of 75 μm and an orifice of diameter 0.200 mm. Both the tube for air and the capillary enter through the face opposite the orifice. After the capillary tube has been aligned with the orifice, the distance H from the tube to the orifice can be simply adjusted by carefully sliding the capillary in its housing on the opposite face to the orifice disk. H is measured with a microscope through the methacrylate face. Fig. 25 shows some views of the feeding tube-orifice set up as seen through the thick methacrylate window (inevitable liquid spills leave behind a debris on the inner face of the window which make the image a bit burr). In particular, Fig. 25 (left) shows the geometry numerically simulated in this work.

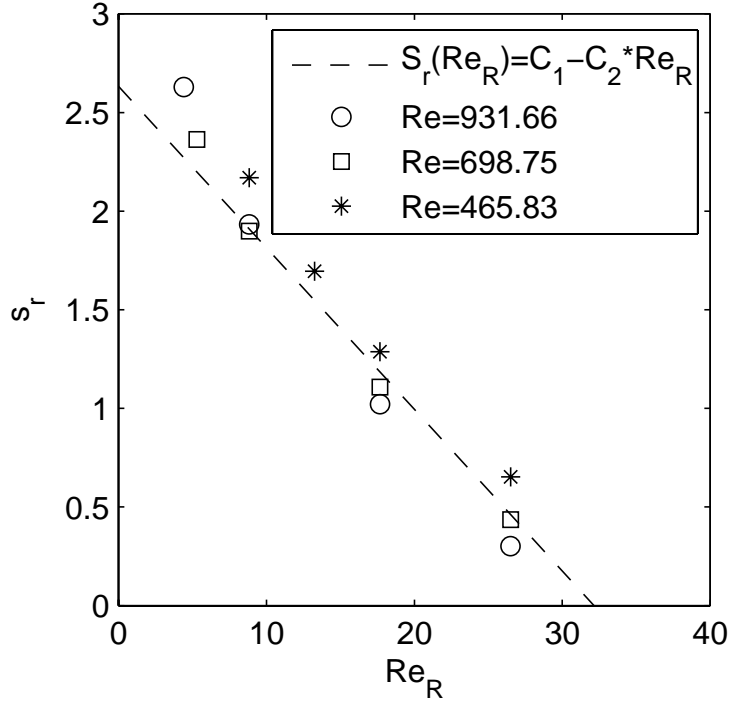


FIG. 23: Recirculation cell size s_r as a function of Re_R : dots, squares and stars are obtained by numerical simulation; the line is a theoretical prediction resulting from dimensional arguments. An additional series of simulations have been performed for an intermediate gas flow condition ($Re = 698.75$ and $We = 18.31$) to assess the validity of the scaling proposed: note the good degree of collapse obtained. The small deviations can be attributable to the small differences in the geometry of the cone for different gas flow conditions.

After setting H and ensuring that the capillary is perfectly coaxial with the nozzle orifice, the pressure is set using a pressure gauge and a pressure meter. A water flow rate is then supplied using a syringe pump (Cole-Palmer 74900 Series) with a 20 ml syringe. The system is allowed sufficient time to relax until either a characteristic stable or unstable flow is present. This can be checked by illuminating the jet that exits the orifice or by looking at the meniscus when the distance H is 0.100 mm or greater. Unstable jet flow appears very faint to the naked eye and contains thin streaks of water along with large scattered spray. This is in significant contrast to stable jet flow, which has bright illumination as a result of a finer, concentrated stream with uniform characteristics. In experiments where the meniscus was visible, it was also possible to discriminate stable versus unstable flow (see Fig.25 (right))

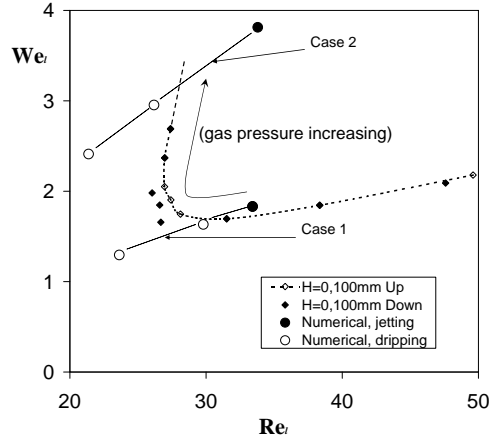


FIG. 24: Jetting -dripping transition in the $\{Re_l, We_l\}$ plane. Diamonds: experimentally determined conditions (filled symbols: liquid flow rate decreasing -“Down”; open symbols: liquid flow rate increasing-“Up”). In most cases, both “Up” and “Down” points coincide). Circles: numerically tested conditions. Filled circles: jetting conditions. Open circles: dripping conditions.

A -jetting- and B -dripping-), in perfect correlation with the spray observations: a stable meniscus had sharp edges and a clear, unwavering glass-like appearance (Fig. 25 A, see steady jet reflected in the metal plate), while an unstable meniscus had blurred edges and flickered (Fig. 25 B, no jet is visible at all). Both the jet test and meniscus test displayed clear and abrupt transitions between the two states. Once unstable flow is established for a given pressure, the rate determined by the syringe pump is increased in steps of 0.1 ml/hr. After each flow rate increase, 30 seconds were waited to ensure that the system had relaxed and all the readings were accurate. This period has been chosen after it was found that 15s was not enough to observe fluctuations in the system: occasionally a stable flow would revert back to unstable flow after the 15s period. The 30s delay has proven long enough to accurately characterize the flow. Accordingly, the rate was increased until the unstable jet sharply transitioned to a stable one; at this point, the flow rate was read from the syringe pump and recorded as the minimal flow rate (increasing, or “up”; Fig. 24). Keeping this same stable flow rate the process is then reversed to find the minimum decreasing (or “down”) flow rate (steps of 0.1 ml/hr and intervals of 30 s until an unstable flow developed). When the flow became unstable, a rate 0.1 ml/hr above the reading on the syringe pump was recorded, since the rate which produced the last stable flow (i.e. minimum flow rate) was

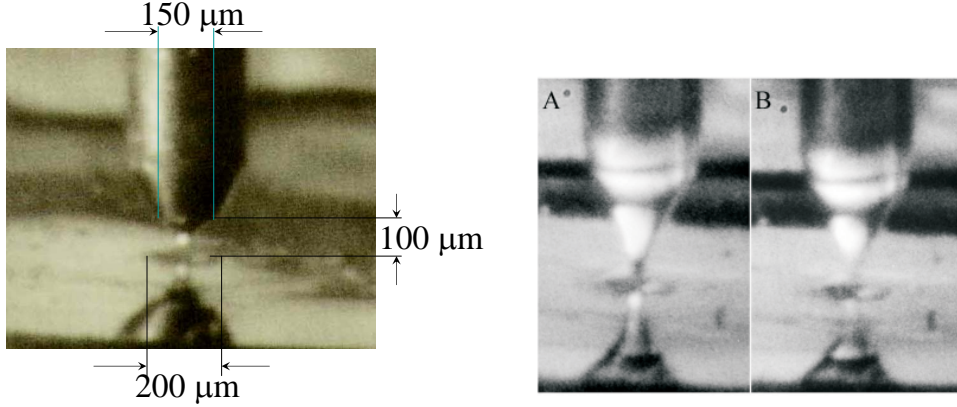


FIG. 25: (Left) Experimental tube-orifice set up as numerically simulated in this work ($D = 200\mu\text{m}$, $D_1 = 150\mu\text{m}$, $H = 100\mu\text{m}$; here, $\Delta P = 10\text{KPa}$, $Q_l = 3\text{ mL/h}$). (Right) Photographs of experimental conditions with twice the distance from the feeding tube to the exit orifice, using a different tube material (fused silica): (A) jetting ($D = 200\mu\text{m}$, $D_1 = 150\mu\text{m}$, $H = 200\mu\text{m}$, $\Delta P = 30\text{KPa}$, $Q_l = 6.1\text{ mL/h}$) and (B) dripping (id. A, with $Q_l = 2.8\text{ mL/h}$).

one step (0.1 ml/hr) higher. The resulting value was recorded as the minimal (decreasing, or “down”) flow rate. This process is repeated for varying pressures and distances of H to get an accurate mapping of minimal jetting flow rates as a function of varying geometry and flow conditions. Following this procedure, we collected the experimental data plotted in Fig. 24 for $H/R = 1$. The gas (air) pressure ΔP increases as indicated by the arrow.

Six conditions numerically tested for cases 1 and 2 are plotted in Fig.24. In order to make our results readily translatable in most of the capillary jet stability literature (which uses the jet radius as a characteristic length), we may introduce liquid Reynolds and Weber numbers consistent with previous definitions and using scaling law (10):

$$Re_l = \left(\frac{2}{\pi^2}\right)^{1/4} \left(\frac{\rho_l^3 Q_l^2 \Delta P}{\mu_l^4}\right)^{1/4}, \quad We_l = \left(\frac{\pi^2}{8}\right)^{1/4} \left(\frac{\rho_l Q_l^2 \Delta P^3}{\sigma^4}\right)^{1/4} \quad (25)$$

As it follows from the plot, using these definitions, jetting or dripping conditions are accurately predicted by the numerical model. This lends additional support to the use of full VOF simulation analysis in flow focusing systems.

VI. CONCLUSIONS

The cone-jet geometry associated with flow focusing has been handled by a diversity of tools, numerical, experimental and theoretical. Order-of-magnitude estimations follow from dimensional arguments: such procedures contribute a valuable theoretical framing and provide the scaling criteria for data representation. Analytical approaches are generally based on the consideration of a perfectly cylindrical infinite jet, a simplification that ignores the influence of the meniscus (a source of instability) and the role of streamline convergence or divergence in the jet. Experiments are burdened by the prolixity of influencing parameters and visualization difficulties associated with the small scale of the meniscus and jet.

In this paper, experimental results are backed up by a numerical simulation based on VOF elements. Numerical schemes allow a more systematic exploration of the parametric influence. In addition, the shortcomings of theoretical models are overcome, and a detailed description of the streamlines can be readily obtained.

The key results of the above exploration are the following:

- The theoretical scaling leading to jet diameter estimates is confirmed by the simulation. The expressions for flow focusing scales, notwithstanding their simplicity, are therefore to be considered a reliable shortcut for the prediction of jet dimensions.
- The complete sequence from meniscus growth to jet emission (jetting regime) and to the sequential filling of drops (dripping regime) is portrayed in detail.
- The jetting-dripping transition is documented in detail, both by experiment and simulation. A two-branch structure is observed in the plot, showing the simultaneous influence of the jet and the meniscus as instability sources. Incipient dripping (Fig. 13) is shown to give rise to highly irregular fluctuations; while fully developed dripping (Fig. 15) produces perfect cycles of drop detachment.
- A recirculation cell is identified in the jetting regime at the meniscus tip. This occurrence appears to be linked to intensive forcing by the gas sheath, leading to high interface velocity along the meridians; the issuing jet is unable to convey all of the mobilized flow, so that a return flow around the axis is observed. The recirculation cell grows as the liquid flow rate is reduced: eventually, dripping conditions are reached.

Similar recirculation cells have been observed in electrospray cones, under thread emission, and in liquid-liquid two-dimensional flow focusing assisted by a surfactant. All of the recirculation instances reported thus far appear to share a common attribute: strong interfacial forcing, either electric, capillary or hydrodynamic.

- A reliable scaling is provided, identifying the parametric conditions where recirculation is to be expected and estimating the size and flow rates of the cell. Controllable recirculation is an extremely attractive feature, providing adjustable residence times within a very simple flow setup. The cell can be viewed as a flow trap or reactor, where biosynthesis or chemical operations take place in a protected environment; the liquid flow rate can be increased to flush the recirculation products.

VII. ACKNOWLEDGMENTS

This work has been supported by the Spanish Ministry of Science and Education, project number DPI2004-07197, and partially supported by European Commission through grant COOP-CT-2005-017725. Thorough discussions of one of the authors (AMGC) with Dr. Joan Rosell are warmly acknowledged.

-
- [1] O. A. Basaran. Small-scale free surface flows with breakup: Drop formation and emerging applications. *AIChE J.*, 48:1842–1848, 2002.
- [2] G. I. Taylor. The formation of emulsions in definable fields of flow. *Proc. R. Soc. London, Ser. A*, 146:501, 1934.
- [3] R. Suryo and O. A. Basaran. Tip streaming from a liquid drop forming from a tube in a co-flowing outer fluid. *Phys. Fluids*, 18:082102, 2006.
- [4] W. W. Zhang. Viscous entrainment from a nozzle: Singular liquid spouts. *Phys. Rev. Lett.*, 93:184502, 2004.
- [5] H. N. Oguz and A. Prosperetti. Dynamics of bubble-growth and detachment from a needle. *J. Fluid Mech.*, 257:111–145, 1993.
- [6] A. M. Gañán-Calvo. Generation of steady liquid microthreads and micron-sized monodisperse sprays in gas streams. *Phys. Rev. Lett.*, 80:285–288, 1998.
- [7] A. M. Gañán-Calvo and J. M. Gordillo. Perfectly monodisperse microbubbling by capillary flow focusing. *Phys. Rev. Lett.*, 87:274501, 2001.
- [8] S. Takeuchi, P. Garstecki, D. B. Weibel, and G. M. Whitesides. An axisymmetric flow-focusing microfluidic device. *Adv. Mater.*, 17:1067–1072, 2005.
- [9] S. L. Anna, N. Bontoux, and H. Stone. Formation of dispersion using flow-focusing in microchannels. *Appl. Phys. Lett.*, 87:364, 2003.
- [10] P. Garstecki, I. Gitlin, W. DiLuzio, E. Kumacheva, H. A. Stone, and G. M. Whitesides. Formation of monodisperse bubbles in microfluidic flow-focusing device. *Appl. Phys. Lett.*, 85:2649, 2004.
- [11] M. Seo, Z. H. Nie, S. Q. Xu, M. Mok, P. C. Lewis, R. Graham, and E. Kumacheva. Continuous microfluidic reactors for polymer particles. *Langmuir*, 21:11614–11622, 2005.
- [12] M. J. Jensen, H. A. Stone, and H. Bruus. A numerical study of two-phase Stokes flow in an axisymmetric flow-focusing device. *Physics of Fluids*, 18, 2006.
- [13] A. S. Utada, E. Lorenceau, D. R. Link, P. D. Kaplan, H. A. Stone, and D. A. Weitz. Monodisperse double emulsions generated from a microcapillary device. *Science*, 308:537–541, 2005.
- [14] C. Berkland, E. Pollauf, D. W. Packa, and K. Kim. Uniform double-walled polymer microspheres of controllable shell thickness. *J. Control. Release*, 96:101–111, 2004.

- [15] Lucía Martín-Banderas, A. Rodríguez-Gil, A. Cebolla, S. Chávez, T. Berdún-Alvarez, J. M. Fernandez-Garcia, M. Flores-Mosquera, and A. M. Gañán-Calvo. Flow focusing: a versatile technology to produce size-controlled and specific-morphology microparticles. *Small*, 1:688–692, 2005.
- [16] L. Martín-Banderas, M. Flores-Mosquera, P. Riesco-Chueca, A. Rodríguez-Gil, A. Cebolla, S. Chávez, and A. M. Gañán-Calvo. Towards high-throughput production of uniformly encoded microparticles. *Adv. Mater.*, 18:559–564, 2006.
- [17] A. M. Gañán-Calvo and P. Riesco-Chueca. Jetting-dripping transition of a liquid jet in a lower viscosity co-flowing immiscible liquid: the minimum flow rate in flow focusing. *J. Fluid Mech.*, 553:75–84, 2006.
- [18] A. M. Gañán-Calvo, M. A. Herrada, and P. Garstecki. Bubbling in unbounded coflowing liquids. *Phys. Rev. Lett.*, 96:124504, 2006.
- [19] A. M. Gañán-Calvo. Absolute instability of a viscous hollow jet. *Phys. Rev. E*, 75:027301, 2007.
- [20] D. Erickson. Towards numerical prototyping of labs-on.chip: modeling for integrated microfluidics devices. *Microfluid Nanofluid*, 1:301–318, 2005.
- [21] V. Cristini and Y.-Ch. Tan. Theory and numerical simulation of droplet dynamics in complex flows-a review. *Lab Chip*, 4:257–264, 2004.
- [22] M. M. Dupin, I. Halliday, and C. M. Care. Simulation of a microfluidic flow-focusing device. *Physical Review E*, 73, 2006.
- [23] M. W. Weber and R. Shandas. Computational fluid dynamics analysis of microbubble formation in microfluidic flow focusing devices. *Microfluid Nanofluid*, 3:195–206, 2007.
- [24] A. Barrero, A. M. Gañán-Calvo, J. Dávila, A. Palacio, and E. Gómez-González. Low and high Reynolds number flows inside Taylor cones. *Phys. Rev. E*, 58:7309–7314, 1998.
- [25] M. A. Herrada and A. Barrero. Self-rotation in electrocapillary flows. *Physical Review E (Statistical, Nonlinear, and Soft Matter Physics)*, 66(3):036311, 2002. URL <http://link.aps.org/abstract/PRE/v66/e036311>.
- [26] S. L. Anna and H. C. Mayer. Microscale tipstreaming in a microfluidic flow focusing device. *Phys. Fluids*, 18:121512, 2006.
- [27] J. M. Fernandez and G. M. Homsy. Chemical reaction-driven tip-streaming phenomena in a pendant drop. *Phys. Fluids*, 16:2548–2555, 2004.

- [28] R. Krechetnikov and G. M. Homsy. On physical mechanisms in chemical reaction-driven tip-streaming. *Phys. Fluids*, 16:2556–2566, 2004.
- [29] For convenience and with the aim of making our results readily reproducible from others, in this work we have used the well tested commercial solver FLUENT v 6.3. Mesh generation is aided by the software GAMBIT in FLUENT v 6.2.
- [30] C.W. Hirt and B.D. Nichols. Volume of fluid (vof) method for the dynamics of free boundaries. *J. Comput. Phys.*, 39:201, 1984.
- [31] P. Heinrich. Nonlinear numerical model of landslide-generated water waves. *Int. J. Engrg. Fluid Mech.*, 4:403, 1991.
- [32] A. Tomiyama, A. Sou, H. Minagawa, and T. Sakaguchi. Numerical analysis of a single bubble by vof method. *JSME Int. J.*, 36:51, 1993.
- [33] B. Lafaurie, C. Nardone, R. Scardovelli, S. Zaleski, and G. Zanetti. Modelling merging and fragmentation in multiphase flows with surfer. *J. Comput. Phys.*, 113:134, 1994.
- [34] B. Van Leer. Toward the ultimate conservative difference scheme. iv. a second order sequel to godunov’s method. *J. Comput. Phys.*, 32:101–136, 1979.
- [35] O. Ubbink. *Numerical prediction of two fluid systems with sharp interfaces*. PhD thesis, Imperial College of Science, Technology and Medicine, London, 1997.
- [36] R. I. Issa. Solution of implicitly discretized fluid flow equations by operator splitting. *J. Comput. Phys.*, 62:40–65, 1986.
- [37] P. Couillet, L. Mahadevan, and C. S. Riera. Hydrodynamical models for the chaotic dripping faucet. *J. Fluid Mech.*, 526:1–17, 2005.
- [38] P. M. Morse and H. Feshback. *Methods of theoretical physics*. McGraw-Hill Pub. Co., 1953.